Maximizing information obtainable by quantum sensors through the quantum Zeno effect

Bruno Ronchi,[1] Analia Zwick,[1,2,3] and Gonzalo A. Álvarez[1,2,3,*]

[1] *Instituto Balseiro, CNEA, Universidad Nacional de Cuyo, S. C. de Bariloche, Argentina*
[2] *Centro Atómico Bariloche, CONICET, CNEA, S. C. de Bariloche, Argentina*
[3] *Instituto de Nanociencia y Nanotecnologia, CNEA, CONICET, S. C. de Bariloche, Argentina*

(Received 17 March 2024; revised 27 July 2024; accepted 28 August 2024; published 25 September 2024)

Efficient quantum sensing technologies rely on the precise control of quantum sensors, particularly two-level systems or qubits, to optimize estimation processes. We here exploit the quantum Zeno effect (QZE) as a tool for maximizing information obtainable by quantum sensors, with a specific focus on the level avoided-crossing (LAC) phenomenon in qubit systems. While the estimation of the LAC energy splitting has been extensively studied, we emphasize the crucial role that the QZE can play in estimating the coupling strength. We introduce the concept of information amplification by the QZE for a LAC system under off-resonant conditions. The proposed approach has implications for ac magnetic field sensing and the characterization of complex systems, including many-spin systems requiring the estimation of spin-spin couplings. Overall, our findings contribute to the advancement of quantum sensing by leveraging the QZE for improved control and information extraction.

DOI: 10.1103/PhysRevApplied.22.034058

I. INTRODUCTION

Developing efficient quantum sensing technologies at atomic and nanometric scales is critically dependent on the precise control of the sensors to enable the achievement of optimal estimation processes [1–14]. The simplest quantum sensor is a two-level system—a qubit—and a variety of experimental designs have been proposed for this purpose [11], including cold atoms [15–17], ion traps [18–20], Rydberg atoms [21,22], polar molecules [22,23], nuclear spins in liquids and solids [4–6,24–30], and nitrogen-vacancy (N-V) centers in diamonds [31–44].

A two-level system can be a subset of many energy levels from a more complex system. Most physical interactions involving two-level systems results in a phenomenon known as a level avoided crossing (LAC) [45]. This happens when the energy levels of the two-level system approach each other without actually crossing, as a result of interactions. The most general Hamiltonian describing a two-level system includes a coupling interaction between the energy levels, facilitating transitions between them, and a "longitudinal" energy offset that creates the energy splitting between the levels.

When employing a two-level system for quantum sensing, it is essential to estimate the relevant interactions, such as the energy offset and/or the coupling between the states [9,11,14]. Accurately characterizing the corresponding LAC Hamiltonian is thus crucial for various applications, including improving spectroscopy techniques [5,46], hyperpolarization in NMR [47–50], N-V center sensors [35,36,41,42,51–55] and in general for developing quantum devices that operate at avoided crossings [56].

While the energy splitting of a two-level system has been extensively studied, and optimal methods for estimating it in different setups have been explored [11,57], the optimization of the estimation procedure for determining the coupling strength between the two energy levels still requires further explorations [35,58–60]. The coupling strength varies due to the qubit's environment and serves as a crucial source of information in several applications, including characterizing spin-spin coupling network topologies [6,14] and time-dependent magnetic fields [11,12,35,61–65].

Quantum estimation tools can provide optimal strategies for efficiently maximizing and extracting information about these relevant parameters [10,11,13,14,66–72]. Depending on the specific parameters, different strategies may be most effective [9]. For example, coherent control may be the optimal strategy for estimating some parameters, while incoherent control techniques such as stroboscopic measurements [6,9,73–76] capable of slowing down the decoherence process, known as the quantum Zeno effect (QZE) [74,77], may be preferable for estimating other parameters [6,9,59,76,78,79].

*Contact author: gonzalo.alvarez@conicet.gov.ar

The QZE can be use to control the transfer of magnetization between spins and significantly amplify the signal emitted by the spins [6,74,80–83]. This manipulation has allowed experimental determination of interactions between spins in networks of many interacting spins [6]. By inducing the QZE through stroboscopic measurements, the system dynamic is simplified from a complex behavior depending on several parameters to a simpler one based on a smaller number of parameters. This simplification allows for a more direct determination of coupling strengths. Complementing these results, quantum information metrics have shown that a quantum probe can more efficiently determine the coupling with its unknown surrounding environment when its dynamic is steered by the QZE [9].

In this work, we explore when stroboscopic projective measurements can enhance the information extraction about the coupling determined by the level avoided crossing. While previous studies suggested limited utility of the QZE for estimating the coupling between states in a LAC Hamiltonian under resonant condition [59], our findings demonstrate that incoherent control, such as stroboscopic projective measurements, can be particularly beneficial when the system is off resonance. We introduce the concept of information amplification by the QZE in a qubit sensor with an offset from resonance, using quantum information tools. This concept includes key elements relevant to more complex systems, such as many-spin systems requiring the estimation of spin-spin couplings for Hamiltonian and/or molecular characterization [6].

II. COUPLING STRENGTH ESTIMATION OF A QUBIT PROBE

The general Hamiltonian

$$H = \frac{1}{2}\boldsymbol{\omega}\cdot\boldsymbol{\sigma}, \tag{1}$$

describes a two-level spin system acting as a qubit probe, where the vector $\boldsymbol{\sigma} = (\sigma_x, \sigma_y, \sigma_z)$ contains the Pauli spin operators, and $\boldsymbol{\omega} = (\omega_x, \omega_y, \omega_z)$ the spin-precession frequency. The intrinsic energy splitting between the spin states $|\uparrow\rangle$ and $|\downarrow\rangle$ is denoted by ω_z considering $\hbar = 1$. For simplicity, we assume $\omega_y = 0$ so as the component ω_x gives the coupling strength between the two qubit states $|\uparrow\rangle$ and $|\downarrow\rangle$. This Hamiltonian provides a universal general form associated with a coupled two-level system, giving rise to a LAC as a function of the energy splitting ω_z, due to the coupling ω_x. The system is on resonance at $\omega_z = 0$, as the population exchange between the states $|\uparrow\rangle$ and $|\downarrow\rangle$ can occur completely. When $\omega_z \neq 0$, it gives the offset of the resonance condition, and the population-exchange probability between the states $|\uparrow\rangle$ and $|\downarrow\rangle$ is attenuated by increasing ω_z.

The density matrix for the two-level system state is

$$\rho = \frac{1}{2}\left[I + \boldsymbol{\mu}\cdot\boldsymbol{\sigma}\right], \tag{2}$$

where $\boldsymbol{\mu}$ is the polarization vector. Initializing the qubit probe with a given polarization on the $\mathbf{z}$ direction $\boldsymbol{\mu}(0) = \mu_0\mathbf{z}$ at time $t = 0$, the qubit state evolves coherently as a function of time t, described by a precession of the polarization vector $\boldsymbol{\mu}$ with the angular frequency $\boldsymbol{\omega}$. Then, the observable is the polarization along the longitudinal axis $\langle\sigma_z\rangle$, which evolves over time depending on the spin-precession frequency $\boldsymbol{\omega}$. Note that μ_0 determines the purity of the initial state, with a pure state corresponding to $|\mu_0| = 1$.

By measuring the observable $\langle\sigma_z\rangle$, the information of the coupling strength ω_x between the two levels $|\uparrow\rangle$ and $|\downarrow\rangle$ is encoded on the evolution of the qubit-state probabilities $p^{\uparrow}(t) = (1 + \mathbf{z}\cdot\boldsymbol{\mu})/2$ and $p^{\downarrow}(t) = (1 - \mathbf{z}\cdot\boldsymbol{\mu})/2$ to obtain $|\uparrow\rangle$ and $|\downarrow\rangle$, respectively. Notice that $\boldsymbol{\mu}$ evolves over time, depending on both the coupling strength ω_x and the offset ω_z. The information about the parameter ω_x is encoded differently depending on whether the qubit sensor undergoes coherent or incoherent dynamics. To determine and quantify the best strategy for estimating the coupling strength ω_x, considering the offset ω_z and the available experimental time, we resort to quantum estimation tools [66–68,84]. The available experimental time is typically constrained by either the decoherence of the quantum probe state, the lifetime of the source generating the coupling, or practical limitations that impose a limit on the total measurement time. We do not explicitly consider the source form inducing these time constraints to simplify and provide a general discussion on amplifying information using the quantum Zeno effect (QZE) and incoherent evolutions. A detailed comparison would depend on the specific form that induces the time constraints. For general results, we treat these constraints as part of the available experimental time for performing the measurements when comparing different estimation protocols.

A. Fisher information of the coupling strength

The minimum attainable error of an unbiased estimation is determined by the quantum Cramer-Rao bound [66–68,84]

$$\delta\omega_x^2 = \langle(\hat{\omega}_x - \omega_x)^2\rangle \geq \frac{1}{N\mathcal{F}_{\mathcal{Q}}(\omega_x)}, \tag{3}$$

where $\hat{\omega}_x$ is the estimated value, N is the number of performed measurements, and $\mathcal{F}_{\mathcal{Q}}(\omega_x)$ is the quantum Fisher

information (QFI) about ω_x. The QFI can be defined as

$$\mathcal{F}_{\mathcal{Q}}(\omega_x) = \sum_n \frac{(\partial_{\omega_x}\lambda_n)^2}{\lambda_n} + 2\sum_{n\neq m}\frac{(\lambda_n-\lambda_m)^2}{\lambda_n+\lambda_m}\left|\langle\lambda_m|\,\partial_{\omega_x}\,|\lambda_n\rangle\right|^2, \quad (4)$$

in the basis of the eigenvectors $|\lambda_n\rangle$ of the density matrix ρ and considering the corresponding eigenvalues λ_n [67]. The QFI can be interpreted as a metric that relates the square of an infinitesimal displacement of the parameter $\mathrm{d}\omega_x^2$ and the square of a statistical distance $\mathrm{d}s^2$ of the induced displacement on the quantum state [66]

$$\mathrm{d}s^2 = \mathcal{F}_{\mathcal{Q}}(\omega_x)\mathrm{d}\omega_x^2. \quad (5)$$

In the case of a evolved state of the two-level system driven by the Hamiltonian of Eq. (1), an infinitesimal displacement in the frequency $d\boldsymbol{\omega}$ and polarization vector $d\boldsymbol{\mu}$ is schematically shown in Fig. 1(a). The QFI of Eq. (4) can be expressed in terms of the polarization vector as

$$\mathcal{F}_{\mathcal{Q}}(\omega_x) = \frac{1}{1-\mu^2}(\partial_{\omega_x}\boldsymbol{\mu}_{\mathrm{r}})^2 + (\partial_{\omega_x}\boldsymbol{\mu}_{\mathrm{t}})^2, \quad (6)$$

where $\partial_{\omega_x}\boldsymbol{\mu}_{\mathrm{r}}$ and $\partial_{\omega_x}\boldsymbol{\mu}_{\mathrm{t}}$ denote the radial and tangential components of the displacement $\partial_{\omega_x}\boldsymbol{\mu}$ (see Appendix A). This means that information about the parameter to be estimated is contained on changes in both the absolute value of the polarization vector and its direction, and this can be altered by controlling its dynamics. In our case, we will show that the projective measurements induce a decoherence process that interacts strongly with the parameter of interest (ω_x).

III. QUANTUM FISHER INFORMATION FOR A QUBIT-PROBE UNDER COHERENT EVOLUTION

We analyze here the estimation protocol when the qubit sensor undergoes a coherent dynamic [9–14,71,85,86]. The QFI of the coupling strength ω_x, obtained by measuring $\langle\sigma_z\rangle$ at time t under a coherent free evolution, is determined by the difference between the polarization trajectories schematized in Fig. 1, following Eq. (6). The dynamics of these polarization trajectories of the qubit-probe state $\boldsymbol{\mu}$ and $\boldsymbol{\mu}+d\boldsymbol{\mu}$, correspond to precessions with frequencies $\boldsymbol{\omega}$ and $\boldsymbol{\omega}+d\boldsymbol{\omega}$, with the couplings ω_x and $\omega_x+\mathrm{d}\omega_x$, respectively [Fig. 1(a)]. Figure 1(c) shows the corresponding qubit-probe polarization μ_z as a function of the evolution time. Since the polarization norm is conserved during the coherent evolution, the first term in Eq. (6) vanishes, and the QFI coincides with the squared euclidean displacement induced on the polarization vector, i.e., the derivative $\partial_{\omega_x}\boldsymbol{\mu}_{\mathrm{r}}(t)=0$ and thus the $\mathcal{F}_{\mathcal{Q}}^{\mathrm{coh}}(\omega_x) = (\partial_{\omega_x}\boldsymbol{\mu}_{\mathrm{t}}(t))^2$. This displacement is induced by two contributions: one due to the change in the norm of the precession frequency and the other due to the change in the precession cone (the precession axis), as shown in Fig. 1(a). The later induces a periodic displacement, becoming maximal at half periods of the precession and null at every period, while the displacement induced by the former grows quadratically as a function of time and defines the more significant contribution to the QFI at long evolution times. More explicitly, the polarization vector at the evolution time t is

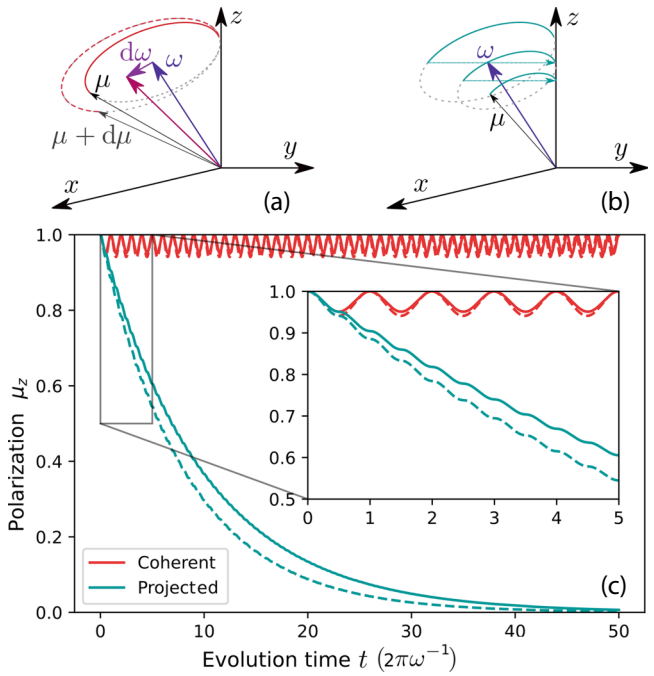

FIG. 1. Comparison of the qubit-probe trajectories of the polarization vector $\boldsymbol{\mu}$ for coherent and projected evolutions for the same precession frequency $\boldsymbol{\omega}$. (a),(b) Polarization vector $\boldsymbol{\mu}$ (black vector) for coherent (solid red line) and projected evolution (solid blue line) for the same precession frequency $\boldsymbol{\omega}$ (violet vector). The dotted lines show the continuation of the polarization trajectory. In the coherent evolution (a), a state trajectory (dashed red line) of the polarization vector $\boldsymbol{\mu}+\mathrm{d}\boldsymbol{\mu}$ (gray vector) is also shown due to a deviation $\mathrm{d}\omega_x$ (violet vector) on the component ω_x of the precession frequency leading to $\omega_x+\mathrm{d}\omega_x$ (purple-red vector). In (b) the polarization vector follows a trajectory driven by a coherent evolution until a nondemolition measurement projects its component on the z axis. (c) Qubit-probe polarization μ_z along the z axis as a function of time t, for the coherent and projected evolutions (red and blue color lines, respectively) with ω_x and $\omega_x+\mathrm{d}\omega_x$ (solid and dashed lines, respectively). We consider an offset ω_z that shows that the exponential decay resulting from a projected evolution induces larger differences between the evolutions corresponding to ω_x and $\omega_x+\mathrm{d}\omega_x$, compared to the differences induced by a coherent evolution. For the schematic plots we use $\boldsymbol{\omega}=2\pi(\cos\theta,0,\sin\theta)$ with $\theta=0.9\pi/2$ being $\omega_z\gtrsim 6\omega_x$, $\mathrm{d}\omega_x=0.1\omega_x$, $\tau=0.5$ and $\boldsymbol{\mu}(0)=z$.

$$\boldsymbol{\mu}(t) = \mu_0 \begin{pmatrix} \frac{\omega_x \omega_z}{\omega^2}(1-\cos(\omega t)) \\ -\frac{\omega_x}{\omega}\sin(\omega t) \\ \frac{\omega_z^2}{\omega^2} + \frac{\omega_x^2}{\omega^2}\cos(\omega t) \end{pmatrix}, \tag{7}$$

where $\omega = |\boldsymbol{\omega}|$. The spin-state polarization on the longitudinal axis is

$$\mu_z(t) = \mu_0 \alpha(t), \quad \alpha(t) = \frac{\omega_z^2}{\omega^2} + \frac{\omega_x^2}{\omega^2}\cos(\omega t), \tag{8}$$

where μ_0 is a constant giving the initial polarization. The longitudinal polarization $\mu_z(t)$ oscillates with an amplitude $\mu_0 \omega_x^2/\omega^2$ with respect to its mean value $\mu_0 \omega_z^2/\omega^2$ as displayed in Fig. 1.

Then, the Fisher information is

$$\begin{aligned} \mathcal{F}_{\mathcal{Q}}^{\mathrm{coh}}(\omega_x) &= \mu_0^2 \left(\frac{\omega_x^2}{\omega^2} t \begin{pmatrix} \frac{\omega_z}{\omega}\sin(\omega t) \\ -\cos(\omega t) \\ -\frac{\omega_x}{\omega}\sin(\omega t) \end{pmatrix} + \frac{\omega_z}{\omega^2} \begin{pmatrix} \frac{\omega_z^2-\omega_x^2}{\omega^2}(1-\cos(\omega t)) \\ -\frac{\omega_z}{\omega}\sin(\omega t) \\ -2\frac{\omega_x \omega_z}{\omega^2}(1-\cos(\omega t)) \end{pmatrix} \right)^2 \\ &= \mu_0^2 \frac{\omega_x^4}{\omega^4} t^2 \left(1 + \frac{2\omega_z^2 \sin(\omega t)}{\omega_x^2 \omega t} + \left(\frac{\omega_z}{\omega_x^2 t} \right)^2 \left[(1-\cos(\omega t))^2 + \frac{\omega_z^2}{\omega^2}\sin^2(\omega t) \right] \right), \end{aligned} \tag{9}$$

which for long times $t \gg \omega_z/\omega_x^2$, takes the approximated form

$$\mathcal{F}_{\mathcal{Q}}^{\mathrm{coh}}(\omega_x) \approx \mu_0^2 \left(\frac{\omega_x}{\omega} \right)^4 t^2, \tag{10}$$

that grows quadratically with time. The accompanying factor $(\omega_x/\omega)^4$ is the fourth power of the cosine of the angle θ between the precession frequency $\boldsymbol{\omega}$ and the $\mathbf{x}$ direction, $\omega_x = \omega\cos\theta$. The QFI as a function of θ and the evolution time shows approximately contoured lines given by the relation $t \propto 1/\cos^2\theta = 1 + (\omega_z^2/\omega_x^2)$, as shown in Fig. 2.

Thus, the QFI of ω_x grows faster as the on-resonance condition is approached and tends to 0 as $\theta \to \pi/2$ by increasing the offset. In this regime of strong offset, the quadratic growth of QFI becomes slow enough that the proposed alternative—projective measurements—provides a better estimation under limited experimental time. While achieving t^2 growth in QFI under coherent evolution is significant, it is worthwhile to note that this does not hold if environmental noise is considered. To address this, we propose adding repeated projective measurements, which can enhance the estimation process when the available experimental time is constrained.

IV. QUANTUM FISHER INFORMATION FOR A QUBIT PROBE UNDER PROJECTED EVOLUTION

We here analyze the estimation protocol when the qubit sensor undergoes an incoherent dynamic via projected evolutions along the z axis. This is achieved through periodic projective—nondemolition—measurements of the observable σ_z at stroboscopic times with a delay τ [6,9,14,73–76,82]. These projective measurements on the two-level system erase the nondiagonal elements of the density matrix in the σ_z basis. This process is referred to as a quantum nondemolition (QND) measurement because it preserves the populations of the system states $|\uparrow\rangle$ and $|\downarrow\rangle$, ensuring that the system's energy, excluding the coupling between the states considered external, remains

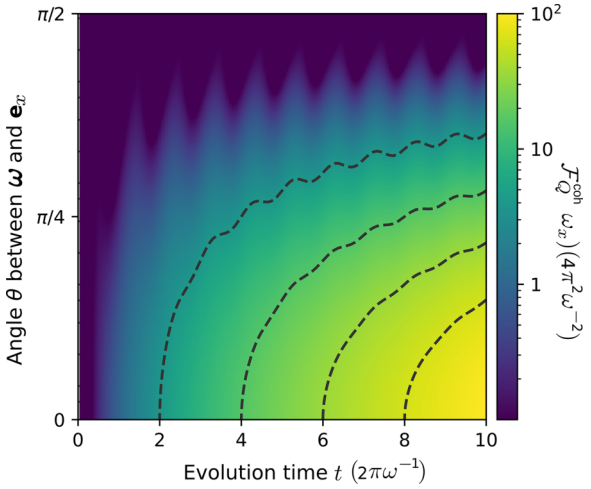

FIG. 2. Quantum Fisher information of ω_x as a function of the evolution time t and of the angle $\theta = \arctan(\omega_z/\omega_x)$ between the precession frequency vector $\boldsymbol{\omega}$ and the direction $\mathbf{x}$ for a coherent evolution from the initial state $\boldsymbol{\mu}(0) = \mathbf{z}$. The dashed lines indicate contour lines that approximately satisfy the relation $t \propto 1/\cos^2\theta$.

unchanged. Notice that the outcomes of QND measurements do not need to be read, as these measurements, as we will see below, are used to guide the evolution of the qubit-probe state. Thus as ideal QND measurements are challenging, experimental realizations often involve applying repetitive random magnetic field gradients [6,82] or employing stochastic processes [87–91] on the qubit-probe system. In the case of magnetic resonance, direct projective measurements are difficult, but they can be replicated using induced dephasing techniques [6,82,88,90–92].

A schematic representation of the probe-state evolution is illustrated in Fig. 1(b). The projective measurements manifest immediately after their application, positioning the qubit-probe polarization along the z axis with its $\mathbf{z}$ component remaining unchanged. The transverse component, representing the nondiagonal terms of the density matrix, is erased by the QND measurement process. However, since these measurements are not selective and do not result in a pure state outcome, following Eq. (7), the total polarization norm is thus reduced by a factor $\alpha(\tau)$, as defined in Eq. (8).

Since the observable is σ_z, for an evolution time t that contains n stroboscopic projective measurements, where $t = n\tau + \Delta t$ with $n \in \mathbb{N}$ and $\Delta t \in [0, \tau)$, the polarization μ_z is given by

$$\mu_z(t) = \mu_0 \alpha(\tau)^n \alpha(\Delta t). \tag{11}$$

At the stroboscopic times $n\tau$, the polarization decays exponentially with the characteristic time

$$t_c = -\frac{\tau}{\ln|\alpha(\tau)|}. \tag{12}$$

The evolution of the polarization $\mu_z(t)$ is shown in Fig. 1(c) for the precession frequencies $\boldsymbol{\omega}$ and $\boldsymbol{\omega} + d\boldsymbol{\omega}$, with the couplings ω_x and $\omega_x + \mathrm{d}\omega_x$, respectively, as in the coherent evolution case. The comparison between the coherent and incoherent evolutions clearly highlights how, under off-resonance conditions, the projected evolution difference between the two cases (ω_x and $\omega_x + \mathrm{d}\omega_x$) is significantly larger than that for the coherent evolution case. This sensitivity of the dynamics against changes in the parameter to be estimated (ω_x) is the main feature we will exploit to improve the inference.

Figure 3(a) shows the decay time t_c as a function of the stroboscopic measurement time τ for $\omega_z \gtrsim 6\omega_x$. A similar qualitative behavior is seen in general for $\omega_z > \omega_x$, as the polarization state $\boldsymbol{\mu}$ does not cross the $\mu_z = 0$ plane during its evolution. As the stroboscopic time $\tau \to 0$, the evolution of the polarization factor $\alpha(\tau) \to 1$ and thus the characteristic decay time $t_c \to \infty$ defining the Zeno regime where the QZE is manifested [74,77]. Figure 3(a) also shows a region for values of τ, where the decay time t_c is minimal corresponding to a anti-Zeno regime [74].

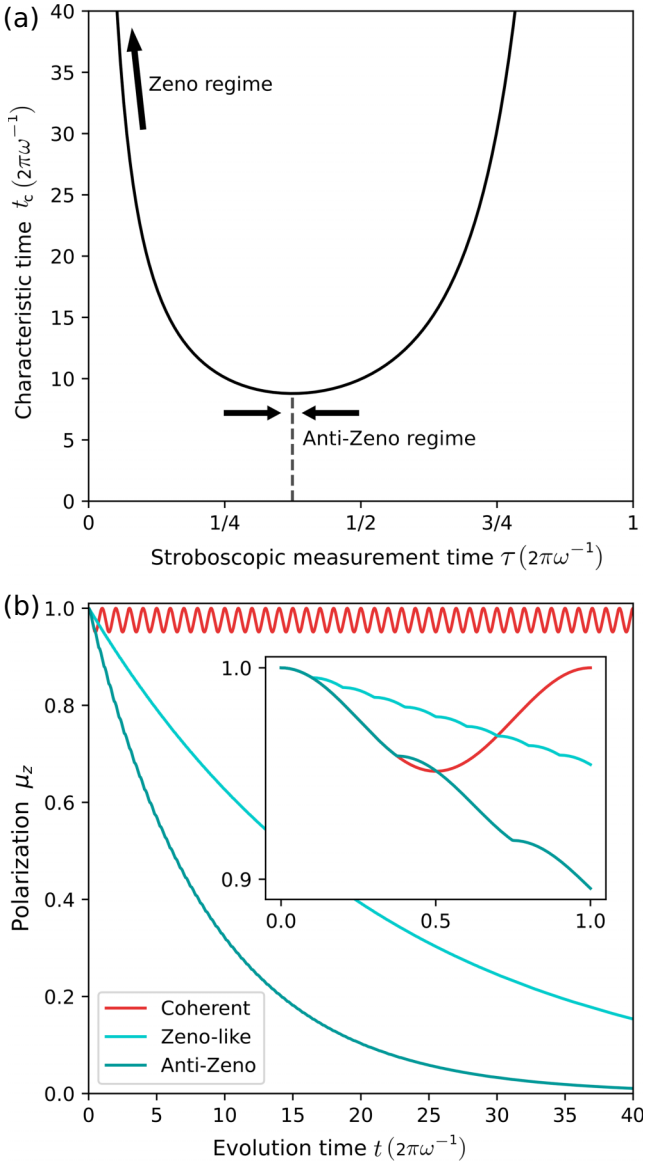

FIG. 3. (a) Characteristic time t_c of a measurement-induced decay as a function of the stroboscopic time τ. The Zeno regime occurs when τ tends to 0, while the anti-Zeno regime occurs for the region where the characteristic time t_c is minimum around $\tau \approx \frac{3}{8}$. For $\omega_z \gg \omega_x$, $t_c \approx \omega^2\tau/2\omega_x^2 \sin^2(\omega\tau/2)$, and the minimum occur for $\omega\tau = \tan(\omega\tau/2)$. (b) Polarization μ_z along the z axis as a function of the total evolution time, for coherent and two projective evolutions corresponding to a Zeno ($\tau = 0.1$) and anti-Zeno regime ($\tau \approx \frac{3}{8}$) (red, blue, and cyan color lines, respectively). Here $\boldsymbol{\omega} = 2\pi(\cos\theta, 0, \sin\theta)$ with $\theta = 0.9\pi/2$ being $\omega_z \gtrsim 6\omega_x$, $\boldsymbol{\mu}(0) = \mathbf{z}$.

These Zeno and anti-Zeno regimes induce the slowest and fastest exponential decay of the polarization μ_z evolution under stroboscopic measurements as shown in Fig. 3(b).

We now calculate the QFI from Eq. (6). Due to the reduction of the polarization norm by the factor $\alpha(\tau)$ at every projective measurement, the first term in Eq.

(6) becomes a piecewise constant evolution. The coherent evolution between the projective measurements contributes to the QFI via the second term of Eq. (6) with a value equal to the one of a coherent evolution after the projection. Thus the second term of the QFI is a coherent contribution that only adds a small quantity on top of the main overall information given by the first term due to the incoherent evolution counterpart. If the stroboscopic time τ is small, $\omega\tau \ll 2\pi$, the first term of the QFI is generated by a decaying incoherent evolution of the qubit state μ_z. The QFI at the stroboscopic times $t = n\tau$ is given only by the radial—first—term in Eq. (6). This is regardless of the value of ω_x, as all trajectories at those specific times are along the z axis [see Fig. 1(b)]. Furthermore, during the coherent evolution between the projective measurements, since the polarization vector conserves its norm, the radial term remains constant, and the second term takes the usual form for a coherent evolution as described in Sec. III, with an initial polarization given by the one obtained at the last projective measurement. Hence, the QFI may be approximated by the first term of Eq. (6) up to a difference of $\mu_0^2\alpha(\tau)^{2n}\Delta t^2$, where Δt is the elapsed time after the last measurement. Considering this approximation, the QFI takes the form (see Appendix B)

$$\mathcal{F}_{\mathcal{Q}}^{\text{proj}}(\omega_x) = t^2\mu_0^2\frac{1}{\tau^2}\frac{\alpha(\tau)^{2(t/\tau-1)}}{1-\mu_0^2\alpha(\tau)^{2t/\tau}}(\partial_{\omega_x}\alpha(\tau))^2. \quad (13)$$

The QFI as a function of time for this projected evolution is represented by a family of self-similar functions parameterized by $\boldsymbol{\omega}$ and τ. Figure 4 shows this QFI of the coupling strength ω_x as a function of stroboscopic time τ and the total evolution time t. The dashed line in Fig. 4(a) shows the maximum value of the QFI $\mathcal{F}_{\mathcal{Q},\max}^{\text{proj}} = \mathcal{F}_{\mathcal{Q}}^{\text{proj}}(t_{\max})$ obtained at $t_{\max}$ that satisfies $\partial_t\mathcal{F}_{\mathcal{Q}}^{\text{proj}}(t_{\max}) = 0$. The maximum QFI occurs at

$$t_{\max} = \xi(\mu_0)t_c, \quad \xi(\mu_0) = 1 + \frac{1}{2}W(-2\mu_0^2/\mathrm{e}^2), \quad (14)$$

where W is the principal branch of Lambert's W function and varies monotonically from 0.79 to 1 as μ_0 goes from 1 to 0. Then the maximum QFI is given by

$$\mathcal{F}_{Q,\max}^{\text{proj}} = \varphi(\mu_0)\frac{t_c^2}{\alpha(\tau)^2}\frac{\omega_x^2}{\omega^2} \times\left[2\frac{1-\cos(\omega\tau)}{\omega\tau}\frac{\omega_z^2}{\omega^2} + \sin(\omega\tau)\frac{\omega_x^2}{\omega^2}\right]^2, \quad (15)$$

$$\varphi(\mu_0) = \mu_0^2\frac{(\xi(\mu_0))^2}{\mathrm{e}^{2\xi(\mu_0)}-\mu_0^2},$$

and the behavior of $F_{Q,\max}^{\text{proj}}(\omega_x)$ as a function of τ is shown in Fig. 4(b).

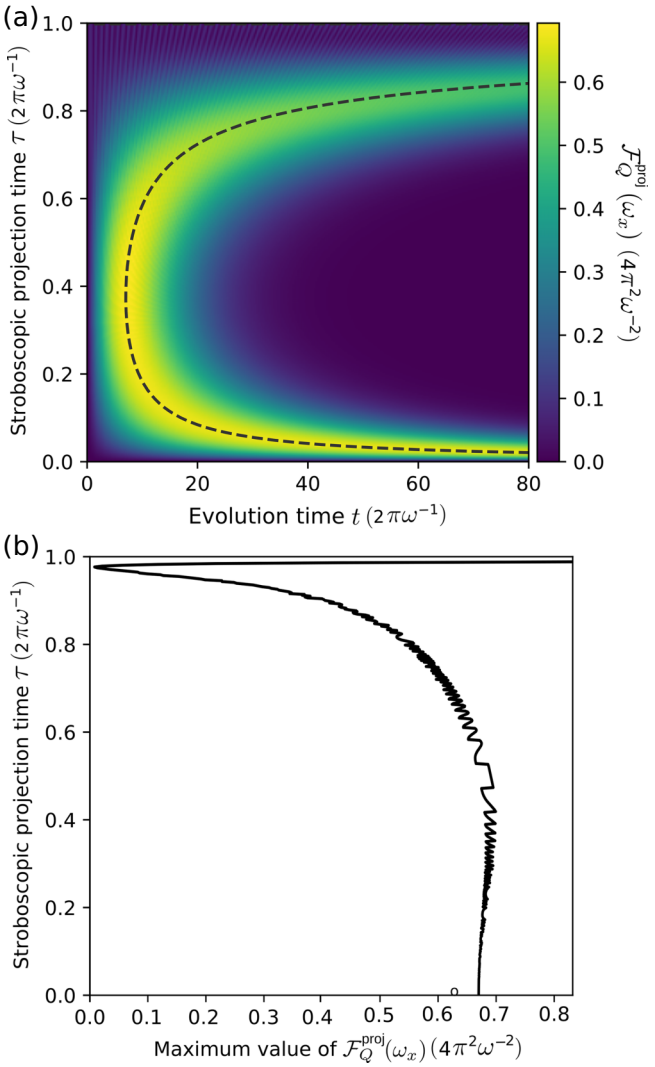

FIG. 4. Quantum Fisher information of the coupling strength ω_x for the projected evolution of the quantum probe. (a) The QFI $\mathcal{F}_{\mathcal{Q}}(\omega_x)$ as a function of the stroboscopic measurement time τ and the total evolution time t. The dashed line shows the maximum value of the QFI $\mathcal{F}_{\mathcal{Q},\max}^{\text{proj}} = \mathcal{F}_{\mathcal{Q}}^{\text{proj}}(t_{\max})$ obtained at $t_{\max}$. (b) Maximum QFI $\mathcal{F}_{\mathcal{Q},\max}^{\text{proj}}$ as a function of τ. The vertical axes in both panels represents the stroboscopic time τ. Parameters used for the plot are $\boldsymbol{\omega} = 2\pi(\cos\theta, 0, \sin\theta)$ with $\theta = 0.9\pi/2$ being $\omega_z \gtrsim 6\omega_x$ and $\boldsymbol{\mu}(0) = \mathbf{z}$. The oscillations in (b) are due to the finite numerical calculations.

Approaching the Zeno regime $\omega\tau \to 0$, $\alpha(t) \approx 1 - \omega_x^2t^2$, and the QFI $\mathcal{F}_{Q,\max}^{\text{proj}} \to 4\varphi(\mu_0)/\omega_x^2$ is a constant value that is obtained at $t_{\max} \approx \xi(\mu_0)/\omega_x^2\tau$, where both are independent of ω_z. This is a key feature of the QZE estimation strategy, as it does not require previous knowledge of the offset ω_z to make an efficient inference. For large offsets $\omega_z \gg \omega_x$, this constant value for $\mathcal{F}_{Q,\max}^{\text{proj}}$ is extended to the anti-Zeno regime requiring less total evolution time to be achieved as can be observed in Fig. 4. Notice that outside the QZE regime, previous knowledge of the offset

is needed for an efficient estimation of the coupling. By continuing to increase τ, the $\mathcal{F}^{\text{proj}}_{Q,\text{max}}$ decreases to zero. This could be related to the manifestation of critical phenomena in the extractable information defining transitions between dynamic regimes of the sensor [10]. Then, $\mathcal{F}^{\text{proj}}_{\mathcal{Q},\text{max}}$ rapidly increases as the evolution approaches the coherent regime, i.e., for $\tau \to 2\pi\omega^{-1}$, but it requires a total evolution time orders of magnitude larger than its anti-Zeno counterpart.

While this discussion addresses the conceptual implications of projective evolution inference and the enhancement for parameter information, specific considerations might need to be accounted for depending on the experimental setup.

To achieve the QZE regime ($\omega\tau \to 0$), projective measurements must be rapid enough to validate the approximation $\alpha(t) \approx 1 - \omega_x^2 t^2$, making the inference of ω_x independent of ω_z. However, since this is an ideal limit, in practical scenarios, we can approach only this regime. When $\omega\tau$ is small but not zero, the approximation of $\alpha(t)$ will have corrections that depend on ω_z. Thus, if ω_z is unknown, the estimation of ω_x will improve as we approach the QZE regime, up to the limit imposed by the uncertainty introduced by these corrections. Additionally, potential errors from the experimental implementation of projective measurements may restrict the total number of stroboscopic measurements to avoid significant accumulated errors. The available measurement time can also limit the ability to achieve optimal inference within the QZE regime. Still, experimental implementations have already demonstrated the benefits of reaching the QZE regime for parameter estimation [6,82]. It is also useful to note that ω_z must always be known for the coherent evolution estimation of ω_x.

The optimal inference generally depends on the true value of the parameter to be estimated [9,14], as seen in Eq. (9) for coherent estimation and in Eqs. (14) and (15) for incoherent estimation, particularly the optimal measurement time. For coherent evolution, this dependency can be mitigated for very long times, as shown in Eq. (10). Note, however, that decoherence effects might prevent attaining this regime.

In many practical scenarios, the parameters we measure, such as ω_x, are typically sampled from a population with known statistical properties. If the variance of ω_x between samples is sufficiently small, the actual t_{max} that optimizes inference will be close to the expected value. Therefore, even without prior knowledge of the true parameter value, the estimation strategy can perform effectively, providing near-optimal information gain. In cases where the parameter to be estimated is completely unknown and exhibits high variance, real-time adaptive estimation protocols can be employed to circumvent this issue [9,14]. These protocols iteratively converge to optimal control and estimation precision bounds without priorknowledge.

It is worth noting that the functional form of $\mathcal{F}^{\text{proj}}_{\mathcal{Q},\text{max}}$ differs from that of the level curves for the QFI in a coherent evolution, as illustrated in Fig. 2 compared to Fig. 4. Specifically, for sufficient large values of ω_z, $\mathcal{F}^{\text{proj}}_{\mathcal{Q},\text{max}}$ becomes constant and defines a contour line that gives the higher information gain at an earlier time compared to the corresponding contour line determined from a coherent evolution. This is the key feature of the projected evolution estimation: when the available experimental time for the measurement is limited, it can attain higher information gain within the available time compared to its coherent counterpart, as we discuss in detail in the next section.

V. MAXIMIZING INFORMATION WITH THE QUANTUM ZENO EFFECT

Here, we compare the estimation efficiency of the coupling strength ω_x, when the qubit probe undergoes coherent and projected (incoherent) evolutions. In the off-resonance regime ($\omega_z > \omega_x$,) the difference between the evolution trajectories of the observable μ_z for a small deviation on the precession frequency ω_x becomes barely distinguishable during coherent evolution [see Fig. 1(c)]. In contrast, projected evolutions lead to larger differences between these trajectories in a region of times before the decaying signal is lost [see Fig. 1(c)]. As previously discussed in Eq. (5), the differences observed in the trajectories resulting from a small deviation in the parameter ω_x provide the valuable information about it. To illustrate this quantitatively, Fig. 5 compares the time-dependent QFI on ω_x between a coherent ($\mathcal{F}^{\text{coh}}_{\mathcal{Q}}$) and projected ($\mathcal{F}^{\text{proj}}_{\mathcal{Q}}$) evolution estimation process, demonstrating a representative functional behavior for a case with a large offset. It reflects the key predicted results of this article: the QFI $\mathcal{F}^{\text{proj}}_{\mathcal{Q}}$ extracted from projected evolutions achieves higher values at shorter times compared to the the QFI information $\mathcal{F}^{\text{coh}}_{\mathcal{Q}}$ extracted from a coherent free evolution when the offset is large $\omega_z > \omega_x$. Specifically, in the example shown in the figure, while $\mathcal{F}^{\text{coh}}_{\mathcal{Q}}$ continuously increases with time, as predicted in Eq. (10), the incoherent evolution reaches its maximum information at a shorter time, approximately $t \approx 6$ (in units of $2\pi\omega^{-1}$). In contrast, the coherent evolution achieves comparable information much later, around $t \approx 27$ (in units of $2\pi\omega^{-1}$).

The $\mathcal{F}^{\text{proj}}_{\mathcal{Q}}$ reaches a maximum and then decays. This occurs because the observable longitudinal polarization μ_z exponentially decays to zero under the QND projective evolutions, reducing the purity of the quantum probe state and consequently the QFI after some time. In contrast, the coherent evolution preserve the polarization magnitude (the state purity) along time, allowing the QFI to increase indefinitely. However, this indefinite growth of the QFI is possible only under ideal conditions where the qubit probe does not experience decoherence.

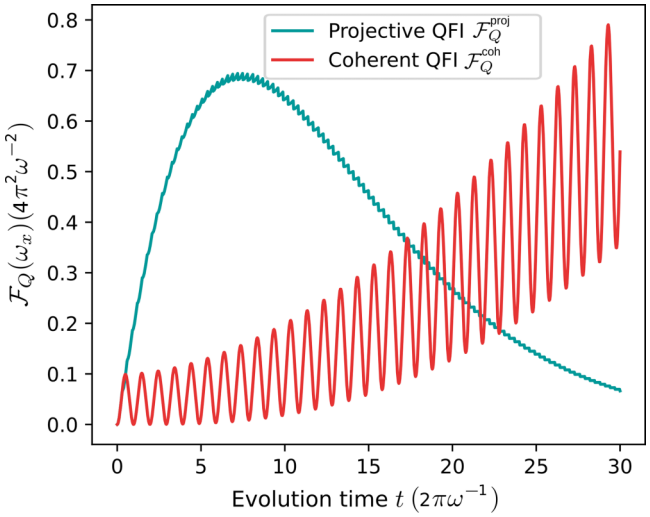

FIG. 5. QFI for a large offset $\omega_z \gtrsim 6\omega_x$ for both coherent and projective evolution estimation. Although the QFI extracted from a coherent evolution yield higher information at long time, the QFI extracted from projective evolution yields a higher value at shorter times. The parameter used for the plot are $\boldsymbol{\omega} = 2\pi(\cos\theta, 0, \sin\theta)$ with $\theta = 0.9\pi/2$ being $\omega_z \gtrsim 6\omega_x$, $\tau = 0.3$ and $\boldsymbol{\mu}(0) = \mathbf{z}$.

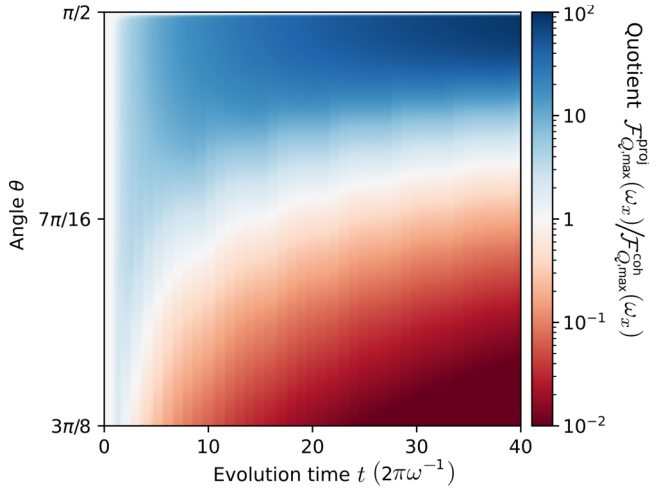

FIG. 6. Quotient of the maximum obtainable QFI for projective and coherent estimation as a function of the angle $\theta = \arctan(\omega_z/\omega_x)$ of $\boldsymbol{\omega}$ with respect to the z axis and total available time t. The white color region represents equal QFI, delineating the boundary where each estimation protocol performs optimally. The quotient was obtained numerically from the exact expressions, and the respective maximum QFI for both evolutions was determined based on the available time. The stroboscopic time τ was varied within the range $[0.08, 0.6]2\pi/\omega$.

In realistic experiments, decoherent effects are always present and are often characterized by the relaxation times T_1 or T_2, which are typically comparable to the precession period $2\pi\omega^{-1}$ or can be 1 to 2 orders of magnitude larger. These relaxation effects reduce the polarization μ_z by an exponential decay factor e^{-t/T_1} or e^{-t/T_2}, depending on the specific setup. Additionally, decoherence sources may be more complex when the environment exhibits a colored spectral density, leading to an interplay between the environment and the qubit probe's coherent and incoherent dynamics [4,14,93]. Specific comparisons would depend on the details of the experimental setup and the system being probed. Therefore, in general, the maximal QFI achievable for given values of ω_x and ω_z is obtained by an optimal trade-off between the ideal information gain from the qubit-probe evolution and the total available time, which is determined by the specific relaxation sources. Thus, achieving the maximal QFI in the shortest possible time is crucial due to decoherence effects on the qubit probe.

Therefore, to provide general conceptual results and avoid specific details that depend on a particular setup, we determine the maximum attainable QFI within the time interval $[0, t]$ for both coherent F_Q^{coh} and projected F_Q^{proj} evolution estimations. We compare them with the quotient $\mathcal{F}^{\text{proj}}_{\mathcal{Q},\max}/\mathcal{F}^{\text{coh}}_{\mathcal{Q},\max}$, where Fig. 6 illustrates the quotient as a function of the angle $\theta = \arctan(\omega_z/\omega_x)$ of $\boldsymbol{\omega}$ with respect to the x axis and the total available time t. Areas colored in white indicate when the quotient is equal to 1, marking the boundary where projected versus coherent evolution is more effective for parameter estimation. For values of ω_z, where the quotient is above 1, the projected evolution estimation is expected to perform better, while it is expected to be less effective when below 1.

For an analytical analysis, we consider the approximations derived above: $\mathcal{F}^{\text{coh}}_{\mathcal{Q},\max}(\omega_x) \approx \mu_0^2(\omega_x/\omega)^4 t^2$ for $t \gg \omega_z/\omega_x^2$ and $\mathcal{F}^{\text{proj}}_{\mathcal{Q},\max} \approx 4\varphi(\mu_0)/\omega_x^2$ for large offsets $\omega_z \gg \omega_x$ and $\tau \lesssim 0.6$. Therefore, the quotient becomes

$$\frac{\mathcal{F}^{\text{proj}}_{\mathcal{Q},\max}}{\mathcal{F}^{\text{coh}}_{\mathcal{Q},\max}} \approx \frac{4\varphi(\mu_0)}{\mu_0^2}\frac{\omega^4}{\omega_x^6}\frac{1}{t^2}, \tag{16}$$

provided that $t \geq t_{\max}$. This expression thus defines the conditions for the optimal estimation at the total available evolution time t. The estimation procedure based on projective measurements on the qubit probe maximize the information about ω_x when the available time is

$$t < \frac{2\sqrt{\varphi(\mu_0)}}{\mu_0\omega_x}\left(1 + \frac{\omega_z^2}{\omega_x^2}\right). \tag{17}$$

In general, this bound depends on the purity of the initial state, but in the limit of low polarization $\mu_0 \ll 1$, $\varphi(\mu_0) = e^{-2}\mu_0^2$, and Eq. (17) approximates to

$$t < \frac{2}{e\omega_x}\left(1 + \frac{\omega_z^2}{\omega_x^2}\right), \tag{18}$$

which is independent of the particular initial polarization μ_0.

Therefore, the dividing boundary curve in Fig. 6 is approximated by the relation $\omega_z \propto \omega_x\sqrt{\omega_x t - 1}$, provided that $t \geq t_{\max}$ and within the regions of the assumptions made. For values of ω_z above this boundary region, the offset is so significant that the contribution of ω_x to the oscillatory dynamics requires more time than is available. Consequently, coherent evolution does not outperform the incoherent decaying dynamics in this regime. Conversely, when the offset is below the boundary region, the oscillatory coherent evolution of the quantum probe is sensitive enough to achieve a higher QFI than what can be attained with incoherent evolution.

This visual representation highlights the key insight from our study: under high off-resonance conditions, projected evolution yields higher QFI at shorter times compared to coherent evolution. This enhancement arises from the interaction between projective measurements and system dynamics, despite the fact that the measurements involve mixed states and reduce state purity over time due to nonselective (QND) projective measurements. The QND measurements induce decoherence that, at shorter times, becomes more sensitive to the parameter ω_x being estimated. This increased sensitivity compensates for the loss of purity, making the measurements more effective. In contrast, while coherent evolution can outperform incoherent evolution given infinite time, the finite experimental time constraints, primarily due to decoherence, make projected measurements more advantageous in certain practical scenarios.

Note that the determined bound for the available time during which incoherent projective evolution outperforms its coherent counterpart does not account for the specific source of decoherence. This bound provides general results based on the available measurement time, offering a broad overview of how incoherent and coherent evolutions compare. For more precise comparisons, detailed information about the decoherence mechanisms and the specifics of the estimation process would be necessary.

VI. APPLICATIONS

In this section we present physical examples that illustrate the advantages of implementing the QZE inference protocol over the coherent strategy. We begin by demonstrating the direct application of inferring ac magnetic fields that are off resonant with the qubit probe. Subsequently, we explore how the same concept can be exploited for inferring spin-spin couplings. In the latter case, we start with the simplest case of a two-spin coupled system, followed by an example illustrating its extension to a three spin system. Finally, we generalize the approach to include many spins.

The incoherent control necessary to achieve the Zeno effects may be applied through QND projective measurements [9]. As discussed in previous sections, the experimental implementation of QND measurements is challenging. However, they can be mimicked through induced dephasing that replicates the effects of QND measurements [6,82,88,91,92,94]. This induced dephasing, which repetitively and stroboscopically projects the qubit state, can be achieved using various methods, including random magnetic field gradients [6,82,92], T_2 relaxation [88], or stochastic interactions [87,89,90]. It is worthwhile to note that the results of QND measurements do not necessitate a readout, as these measurements solely guide the evolution of the qubit-probe state.

In practical quantum sensing applications, such as magnetic field sensing, environmental noise and methods to mitigate its effects are critical for optimizing measurement performance. One effective strategy is the use of dynamical decoupling sequences, which enhance coherence times by reducing the impact of noise and unwanted interactions with the environment [8,26,95]. This technique can significantly improve the QFI and overall sensitivity of the measurement [9,11,14,35,72]. The best overall sensing strategy strongly depends on the specific experimental implementation [8,11]. Although our current work primarily explores theoretical and conceptual frameworks without incorporating these specific techniques and details, the specific implementation will generally impose a finite available experimental time for performing the inference. Thus, we perform a general analysis based on imposing a constraint on the available time for inferring the coupling strength parameter ω_x.

The implementation of QND measurements may induce additional errors due to experimental limitations. If these errors are significant, they will cause a faster decay of the incoherent evolution, reducing inference efficiency. These factors need to be considered to determine the optimal inference framework, as they will change the boundary between the parametric regions where projected or coherent evolution is more efficient for parameter estimation according to Eq. (16).

Therefore, if a strict analysis is required, for example, to push the precision limits of parameter inference, all details would need to be accounted for. However, here we focus on the overall comparison between coherent and incoherent estimation based on a general constraint on the measurement available time.

A. Sensing an off resonant, external ac magnetic field with a 1/2 spin

We consider a $1/2$ spin interacting with a homogeneous and static magnetic field $\mathbf{B}_0 = B_0\mathbf{z}$ as the qubit probe. It thus precesses with the Larmor frequency $\omega_0 = \gamma B_0$ around the z axis, where γ is the gyromagnetic ratio. The qubit probe is treated as a magnetometer for estimating an ac magnetic field along the x axis, determined by $\mathbf{B}_1(t) = 2B_1\cos(\omega t)\mathbf{x}$, where ω is the carrier frequency

and B_1 is the field strength [11,35,38–40,43,44]. In the rotating frame precessing at the angular frequency ω, and under the rotating-wave approximation [96], the spin interacts with an effective magnetic field $(\omega_0 - \omega)/\gamma \mathbf{z} + B_1 \mathbf{x}$. Here, we have assumed that $B_0 \gg B_1$ and that the offset $\omega_z = \omega_0 - \omega$ is much lower than the Larmor frequency $|\omega_z| \ll \omega_0$.

This interaction can thus be mapped to the general two-level system Hamiltonian of Eq. (1), where $\omega_x = \gamma B_1$, $\omega_y = 0$ and the offset $\omega_z = \gamma B_0 - \omega$ defines how far the ac field is from the on-resonance condition.

Following the results derived in Eqs. (16)–(18), we can determine when the projective measurements protocol for estimating the ac field strength $\omega_x = \gamma B_1$ provides a better approach compared to a coherent evolution if the available total measurement time is t. We thus obtain that if t satisfies

$$t < \frac{2}{e} \frac{B_1^2 + (B_0 - \omega/\gamma)^2}{B_1^3}, \tag{19}$$

projective measurement outperforms a coherent evolution estimation protocol. This regime is useful when the on-resonance condition cannot be fulfilled, which might occur when either ω or B_0 cannot be controlled to put the qubit probe on resonance. For example, this circumstance could arise when using an ensemble of spins that feel different magnetic fields B_0, leading to an intrinsic large offset value. This condition can arise in nuclear magnetic resonance (NMR) experiments using a mouse magnet that is placed at the side or near the surface of the sample to be studied, causing the B_0 field to be spatially inhomogeneous within the sample, leading to a broadening of the NMR spectrum [97].

B. Sensing spin-spin couplings

The estimation of the coupling strength between interacting spins is a crucial experimental challenge in chemistry for characterizing molecular topology and various quantum technologies [6,11,33,90,98–101]. This is particularly relevant for Hamiltonian characterization [6,11,44,90,99,100] as well as the improvement of spectroscopy techniques [5,38–40,43,46], optimization of hyperpolarization in N-V centers [36,41,51–55] and NMR [47–50], cross polarization [102–108], the characterization of molecular structures with NMR that define physicochemistry properties or internuclear distances [6,33,96,109], among others.

1. Two-spin coupling

To illustrate the introduced inference method, we focus on estimating the coupling strength and inferring the Hamiltonian of two interacting spins systems. Specifically, we consider a two-spin coupled system during a cross-polarization experiment in NMR [109,110]. This technique is useful for transferring magnetization from a system with high abundance and/or polarization (spin I), such as ^1H, to a system of low abundance and/or small gyromagnetic factor γ (spin S), like ^{13}C. The two spin species are subjected to a static magnetic field B_0 as in the previous example.

The Zeeman interaction defines the resonance frequencies of each spin $\omega_{0,i} = \gamma_i B_0$ where $i = I, S$, typically in the order of hundreds of MHz and differing also in that order. The dipolar interaction between the spins is in the order of kHz, making the polarization and magnetization exchange between them negligible. To generate the polarization exchange (cross polarization), it is necessary to put the two spin species on resonance. For that, oscillating magnetic fields $\mathbf{B}_{1,i}(t)$ of frequencies $\omega_{0,i}$ $(i = I, S)$ are applied. In the high radio-frequency field regime where $|\omega_{1,I} + \omega_{1,S}| \gg |b|$ with $\omega_{1,i} = \gamma_i B_{1,i}$ and $B_{1,i} = \max |\mathbf{B}_{1,i}(t)|$, a secular approximation can be done [109]. This yields the interacting Hamiltonian in the double rotating frame precessing at the two spin frequencies

$$H = -\frac{1}{2}\Delta (S_z - I_z) + b \left(S_x I_x + S_y I_y\right). \tag{20}$$

Here $I_v = \frac{1}{2}\sigma_{v,I}$ and $S_v = \frac{1}{2}\sigma_{v,S}$ are the spin operators with $v = x, y, z$, $\Delta = \left(\omega_{1,S} - \omega_{1,I}\right)$ is the off-resonant energy, and the dipolar interaction is

$$b = -\frac{1}{2}\left(\frac{\mu_0 \gamma_I \gamma_S}{4\pi r^3}\right) \frac{3r_z^2 - r^2}{r^2}, \tag{21}$$

where r is the modulus of the internuclear distance vector, and r_z its z component. Then, the on-resonance condition for achieving a full cross polarization, called the Hartmann-Hahn condition [110], is $\Delta = 0$.

The sample is initially polarized by the action of the static field $B_0 \mathbf{z}$. The polarization in the insensitive species S is typically negligible or removed for quantitative analysis, so only the sensitive species I is polarized along z axis according to the Boltzmann distribution. The initial state is diagonal in the Zeeman basis, and as the Hamiltonian of Eq. (20) conserves the total magnetization on the z axis, the evolution of the spins takes place within density-matrix blocks conserving the total magnetization $S^z + I^z$. The matrix blocks of the spaces $\{\uparrow\uparrow\}$ and $\{\downarrow\downarrow\}$ do not generate dynamics in the system, so their populations are constant over time. The dynamics occur only on the subspace of the Zeeman states $\{\uparrow\downarrow, \downarrow\uparrow\}$, subject to the effective Hamiltonian

$$\frac{1}{2}\begin{pmatrix} -\Delta & b \\ b & \Delta \end{pmatrix}. \tag{22}$$

This Hamiltonian is equivalent to Eq. (1), with an angular frequency

$$\boldsymbol{\omega} = \frac{1}{\hbar}(-b, 0, \Delta), \tag{23}$$

with a Pauli operator $\boldsymbol{\sigma}_{\uparrow\downarrow}$ acting on the two-state subspace $\{|\uparrow\downarrow\rangle, |\downarrow\uparrow\rangle\}$. Then, the process to estimate the coupling strength b is analogous to the estimation of ω_x with an offset $\omega_z = \Delta$ as discussed in the previous sections.

Since the blocks of the spaces $\{\uparrow\uparrow\}$ and $\{\downarrow\downarrow\}$ are static, they do not contribute to the QFI of any parameter. Only the state in the block of space $\{\uparrow\downarrow, \downarrow\uparrow\}$ contributes to the QFI. In this two-level space, with a trace of $\frac{1}{2}$, the polarization vector is defined by

$$\rho_{\uparrow\downarrow} = \frac{1}{4}\left[I_{\uparrow\downarrow} + \boldsymbol{\mu}\cdot\boldsymbol{\sigma}_{\uparrow\downarrow}\right], \tag{24}$$

where the subscript $\uparrow\downarrow$ indicates that the operators act on the subspace generated by $\{|\uparrow\downarrow\rangle, |\downarrow\uparrow\rangle\}$. The initial condition is

$$\boldsymbol{\mu}(t=0) = \left(\frac{\exp\left(-\frac{1}{2}\frac{\omega_{0,I}}{kT}\right)}{\cosh\left(-\frac{1}{2}\frac{\omega_{0,I}}{kT}\right)} - 1\right)\mathbf{z} \tag{25}$$

$$\approx -\frac{1}{2}\frac{\omega_{0,I}}{kT}\mathbf{z}, \tag{26}$$

where this last approximation corresponds to the high-temperature limit, valid for NMR experiments at room temperature [96]. Thus the polarization vector precesses with the angular frequency, leading to an evolution for its z component given by

$$\mu_z(t) = \frac{1}{2}\mu_0\frac{\Delta^2 + b^2\cos\left(\sqrt{b^2+\Delta^2}t\right)}{\Delta^2 + b^2}. \tag{27}$$

This polarization component represents the magnetization exchange between the spins, whose polarization transfer amplitude is $b^2/\left(\Delta^2 + b^2\right)$. Therefore, an off-resonant offset Δ far from the Hartmann-Hahn condition reduces the information gain for the estimation of b based on the free coherent evolution of the system. For an off-resonant exchange of polarization, with large offset Δ, projective measurements applied on the spins on the z axis lead to a more efficient estimation of the coupling strength b if the available total evolution time satisfies

$$t < \frac{2}{\mathrm{e}}\frac{b^2+\Delta^2}{b^3} = \frac{2}{\mathrm{e}}\frac{b^2 + \left(\omega_{1,I}+\omega_{1,S}\right)^2}{b^3}, \tag{28}$$

according to Eqs. (16)–(18). Typically the coherent evolution decoheres due to interactions with the environment, imposing restrictions to the available time for the inference [102,103,111].

The impossibility of generating the Hartmann-Hahn condition occurs in many experimental situations, particularly in cases of very complex spectra, such as spin ensembles with different resonance frequencies, as is the case of solid-state systems with polycrystalline samples [104–106]. In such cases, it is convenient to use the estimation method based on exploiting projective evolutions, which can be implemented with magnetic field gradients, as shown in Ref. [6,82,92]. Regardless of choosing the optimal way to estimate the coupling between the spins, working in the QZE regime using projective measurements allows us to estimate the coupling selectively without needing to know the offset of the Hartmann-Hahn condition. This is a great advantage in these complex systems.

2. Three-spin couplings

We now extend our focus to estimating the interacting couplings among three spins. Specifically, we assume one spin S and two spin I again in the presence of a static field B_0 in the $\mathbf{z}$ direction and radiofrequency fields $B_{1,I}$ and $B_{1,S}$ in the $\mathbf{x}$ direction. The dipolar couplings between S and both spins I are denoted as b_k, $k = 1, 2$, while the coupling between the spins I is denoted as d. For a three-spin system, as in an extended cross-polarization experiment, S represents for example a ^{13}C nucleus and the two spins I, e.g., two protons ^{1}H [102,104,106–108]. The dipolar couplings between the proton k and the carbon are

$$b_k = -\frac{1}{2}\left(\frac{\mu_0\gamma_I\gamma_S}{4\pi r_{(k)}^3}\right)\frac{3r_{(k)z}^2 - r_{(k)}^2}{r_{(k)}^2}, \quad k = 1, 2, \tag{29}$$

and the coupling between the protons is

$$d = -\frac{1}{2}\left(\frac{\mu_0\gamma_I^2}{4\pi r^3}\right)\frac{3r_z^2 - r^2}{r^2}. \tag{30}$$

Similar to the two coupled spins case (Sec. VI B 1), the Hamiltonian in the double rotating frame preserves the total magnetization of the system along the respective directions of the radiofrequency fields. The Hamiltonian again acquires a block structure defined by the total magnetization along z of the full system $M = M_I + M_S$, where $M_I = M_1 + M_2$ is the total magnetization of the protons along z with M_1 and M_2 being the z magnetization of each proton, and M_S is the z magnetization of the ^{13}C. The Hamiltonian induces transitions only between states of the form $\{|M_I, M_S\rangle\}$ and $\{|M_I \pm 1, M_S \mp 1\rangle\}$.

Symmetric and antisymmetric states, $|S\rangle$ and $|A\rangle$, respectively, are defined in the proton Zeeman basis as

$$|S\rangle = \frac{1}{\sqrt{2}}(|+,-\rangle + |-,+\rangle), \tag{31}$$

$$|A\rangle = \frac{1}{\sqrt{2}}(|+,-\rangle - |-,+\rangle). \tag{32}$$

Within the total Zeeman subspace

$$\{|S\rangle\otimes|+\rangle, \quad |+,+\rangle\otimes|-\rangle, \quad |A\rangle\otimes|+\rangle\},$$

$$[H]_{M=\frac{1}{2}} = \begin{pmatrix} \frac{1}{4}(\Sigma-\Delta)+\frac{1}{2}d & \frac{\sqrt{2}}{8}(b_1+b_2) & 0 \\ \frac{\sqrt{2}}{8}(b_1+b_2) & \left(\frac{1}{4}\Sigma+\frac{3}{4}\Delta\right)-\frac{1}{4}d & \frac{\sqrt{2}}{8}(b_2-b_1) \\ 0 & \frac{\sqrt{2}}{8}(b_2-b_1) & \frac{1}{4}(\Sigma-\Delta) \end{pmatrix}. \tag{33}$$

There are several realistic situations where the conditions $b_1 = b_2 = b$ or $b_1 = -b_2 = b$ hold, as it is the case determined by the symmetries of the liquid crystal n-octyl-cyanobiphenyl liquid crystal (nCB) molecules [102]. Therefore, for simplicity, we consider the case of $b_1 = b_2$, where we see that the transitions between $|+,+\rangle \otimes |-\rangle$ and $|A\rangle \otimes |+\rangle$ vanish. In this case, we obtain a polarization dynamics between only two levels dictated by the effective Hamiltonian

$$\begin{pmatrix} \frac{1}{4}(\Sigma-\Delta)+\frac{1}{2}d & \frac{\sqrt{2}}{4}b \\ \frac{\sqrt{2}}{4}b & \left(\frac{1}{4}\Sigma+\frac{3}{4}\Delta\right)-\frac{1}{4}d \end{pmatrix}. \tag{34}$$

Except for a constant component, this corresponds to a Hamiltonian like the one considered in Eq. (1). Here, $\omega_x = -\frac{\sqrt{2}}{2}b$ depends on the dipolar coupling between the protons and the carbon, and $\omega_z = \frac{1}{2}\Delta - \frac{3}{8}d$ depends on the offset and the proton-proton interaction. For the case $b_1 = -b_2$, exactly the same result is obtained within the the Hamiltonian block $M = -\frac{1}{2}$ [102]. The proposed method can be implemented for estimating the heteronuclear dipolar coupling b when the interaction between the protons is large, or if we do not know it and we want to estimate the coupling b regardless of the knowledge of d. Moreover, the projective methods can also be useful for off-resonant polarization transfers, as discussed in the previous Sec. VI B 1.

As described in Eqs. (16)–(18), for a large offset ω_z, projective measurements become more efficient for the estimation of b compared with coherent evolutions if the total available measurement time is bounded by $t < 2/\mathrm{e}(\frac{1}{2}b^2 + \left(\frac{1}{2}\Delta - \frac{3}{8}d\right)^2/\frac{\sqrt{2}}{4}b^3)$. For the case $b_1 = -b_2$ a similar result is obtained.

3. Generalization to many-spin systems

The general properties for the comparison between estimation under coherent and projective evolutions are not dependent of the details of the quantum dynamics. Analogous to the case of two-level systems, coherent and projective estimations are defined mainly by the second and the first sum of Eq. (4), respectively. Coherent estimation provides a QFI that, in general terms, evolves with the square of the product between the evolution time and a factor dependent on the parameter to be estimated [see Eq. (10)]. Similarly, the QFI extracted from projective evolutions arises from the exponential decay of a spin observable dynamics. Thus, optimal evolutions are expected to be approximated by the characteristic decay time induced by the stroboscopic measurements' approach [see Eq. (12)]. In general, the parameter values at which the QZE estimation approach becomes advantageous over the coherent approach, are when the transition exchange probability between the relevant states is significantly reduced. Yet, a key advantage of the QZE approach is that the dependency of several parameters of the dynamics is further simplified by the projective evolutions, as exploited in Ref. [6]. This simplification facilitates the estimation of couplings strengths between spins, enabling the determination of the spin-spin coupling network topology in many-body spin system. Coherent evolution is generally very complex and difficult to use practically for determining the entire coupling structure [6,90,98,99,101].

Here we demonstrate the implementation of a QZE estimation protocol as a tool for inferring spin-spin couplings in many-spin systems. To illustrate this phenomenon, we consider the Trotter-Suzuki expansion to determine the quantum dynamics at short times, where the QZE approach is manifested and becomes useful.

We consider a Hamiltonian with an isotropic interaction between the spins as used in Ref. [6] to showcase the extension of our approach for estimating the couplings strengths between spins in many-body systems. However, the results discussed here are valid for Heisenberg-type interactions. The Hamiltonian is

$$H = \sum_i \omega_i^z I_i^z + \sum_{i<j} b_{ij}\, \mathbf{I}_i \cdot \mathbf{I}_j, \tag{35}$$

where i indexes the spins and b_{ij} are the coupling strengths between spins i and j. The evolution operator can be expanded using a first-order Trotter-Suzuki expansion at short time to lead

$$U(t) = \mathrm{e}^{-iHt} \approx \prod_i \mathrm{e}^{-it\omega_i^z I_i^z} \prod_{i<j} \mathrm{e}^{-itb_{ij}\, \mathbf{I}_i \cdot \mathbf{I}_j}. \tag{36}$$

If the initial condition is given by $\rho(0) = 1 + \mu_0 I_i^z$, its quantum evolution will be determined by the evolution of the operator I_i^z. At short times $t \ll b_{ij}^{-1}$, $(\omega_i^z - \omega_j^z)^{-1}$ its evolution is given by

$$I_i^z \to I_i^z \left(1 - \sum_{j\neq i} \frac{b_{ij}^2 t^2}{8}\right) + \sum_{j\neq i} I_j^z \frac{b_{ij}^2 t^2}{8} + \mathcal{O}, \tag{37}$$

where $\mathcal{O}$ represents higher Trotter-Suzuki expansion orders in time, and nonobservable or observable terms by

monitoring the evolution of I_i^z by nondemolition measurements [6]. The dynamic observed from the initially excited spin $\mathrm{Tr}\left[\rho(t)I_i^z\right]$, in this short time regime, can be mapped to one given by a central spin i homogeneously coupled to the remaining spins j, with an effective interaction $b = \sqrt{1/N\sum b_{ij}^2}$ where N is the number of spins [112]. Then, the spins j can be decimated to a single effective spin following the protocol described in Ref. [113], thus allowing a reduction of the dynamics to one described by an effective two-spin system. Therefore, within this quantum Zeno regime $\omega_i^z\tau, b_{ij}\tau \to 0$, $\alpha(t) \approx 1 - b^2t^2/8$ and the QFI is maximized at $\mathcal{F}_{\mathcal{Q},\max}^{\mathrm{proj}} \to 32\varphi(\mu_0)/b^2$ by measuring the spin state I_i^z at the total evolution time $t_{\max} \approx 8\xi(\mu_0)/b^2\tau$. This is an key feature of this QZE estimation strategy, as it does not require previous knowledge of the offsets ω_i^z and the couplings b_{jl} with $j \neq l \neq i$ to make the inference efficient.

VII. CONCLUSIONS

In summary, our study into the potential exploitation of the quantum Zeno effect to maximize information for quantum sensors represents a step forward in quantum sensing technologies. Focusing on the general features of the level-avoided-crossing phenomenon in two-level systems as a paradigm defining the Hamiltonian of the quantum sensor, underscores the significance of the QZE in estimating the coupling strength—a parameter essential for various quantum sensing applications.

We introduce the concept of information amplification by the QZE, particularly in off-resonant conditions. Our findings reveal that incoherent control, specifically through stroboscopic projective measurements, may outperform coherent strategies for coupling strength estimation, especially when facing time constraints due to decoherence. The use of the quantum Fisher information as a metric for inference strategies sheds light on the nuanced dynamics between coherent and incoherent evolution in qubit-probe systems. Notably, our results indicate that, under time constraints imposed by decoherence, the incoherent strategy exhibits superior performance for large offsets.

A key finding of our study is that under high off-resonance conditions, projected evolution can yield higher quantum Fisher information in shorter timeframes compared to coherent evolution. This advantage stems from the interaction between projective measurements and system dynamics, where QND measurements induce a kind of relaxation that enhances sensitivity to coupling strength at shorter times. While coherent evolution may outperform incoherent evolution over infinite time, practical experimental constraints—primarily due to decoherence—make projected measurements more advantageous in specific scenarios.

We show practical applications supporting the advantages of the proposed QZE inference protocol. We demonstrate its effectiveness in inferring off-resonant ac magnetic fields and spin-spin couplings, offering examples from two-spin to many-spin systems.

One of the key outcomes of our work is that achieving the quantum Zeno regime enables selective inference of coupling strengths. This strategy simplifies the qubit-probe dynamics and the inference procedure by filtering out the complexity of the full system. For instance, we demonstrate that in this regime, prior knowledge of the offset or non-first-neighbor spin-spin coupling to the sensor is not required.

The implementation of incoherent control, leveraging QND projective measurements and induced dephasing, emerges as a versatile tool for steering qubit-probe evolution. The results of QND measurements, crucial for guiding the system's dynamics, do not necessitate readout, allowing emulation through various methods, such as induced dephasing via random magnetic field gradients, T_2 relaxation, or stochastic interactions.

In essence, our work aims to contribute to the ongoing development of quantum sensing methodologies, providing insights for optimizing quantum sensor performance. By exploring incoherent control and strategically choosing parameters, we hope our approach will open alternative possibilities for enhancing quantum sensing capabilities across different applications. Our findings, contribute to the collective efforts in precision-measurement techniques and lay the groundwork for potential advancements in quantum technology.

ACKNOWLEDGMENTS

This work was supported by CNEA; CONICET; ANPCyT-FONCyT PICT-2017-3156, PICT-2017-3699, PICT-2018-4333, PICT-2021-GRF-TI-00134, PICT-2021-I-A-00070; PIBAA 2022-2023 28720210100635CO, PIP-CONICET (11220170100486CO); UNCUYO SIIP Tipo I 2019-C028, 2022-C002, 2022-C030; Instituto Balseiro; Collaboration programs between the MINCyT (Argentina) and MOST (Israel). B.R. acknowledges support from the Instituto Balseiro (CNEA-UNCUYO). A.Z. and G.A.A. acknowledge support from CONICET.

APPENDIX A: QUANTUM FISHER INFORMATION AS A FUNCTION OF THE POLARIZATION VECTOR

Starting from the QFI given by Eq. (4), we derive the QFI in terms of the polarization vector [Eq. (6)]. The density matrix ρ, given by Eq. (2), is diagonalized by the vectors

$$\left|\frac{1+\mu}{2}\right\rangle = \cos\left(\frac{\theta}{2}\right)|\uparrow\rangle + e^{i\varphi}\sin\left(\frac{\theta}{2}\right)|\downarrow\rangle\,, \tag{A1}$$

$$\left|\frac{1-\mu}{2}\right\rangle = \mathrm{e}^{-i\varphi}\sin\left(\frac{\theta}{2}\right)|\uparrow\rangle - \cos\left(\frac{\theta}{2}\right)|\downarrow\rangle, \tag{A2}$$

with eigenvalues $\frac{1}{2}(1+\mu)$ and $\frac{1}{2}(1-\mu)$, respectively, where μ is the magnitude, and θ and φ are the azimuthal and polar angles of $\boldsymbol{\mu}$.

The term related to the mixing of the QFI, Eq. (4), takes the form:

$$\sum_{n:\lambda_n\neq 0}\frac{(\partial_{\omega_x}\lambda_n)^2}{\lambda_n} = \frac{\left(\partial_{\omega_x}\left(\frac{1+\mu}{2}\right)\right)^2}{\frac{1+\mu}{2}} + \frac{\left(\partial_{\omega_x}\left(\frac{1-\mu}{2}\right)\right)^2}{\frac{1-\mu}{2}} \tag{A3}$$

$$= \frac{1}{2}\left(\partial_{\omega_x}\mu\right)^2\left(\frac{1}{1+\mu}+\frac{1}{1-\mu}\right) \tag{A4}$$

$$= \frac{\left(\partial_{\omega_x}\mu\right)^2}{1-\mu^2} = \frac{\left(\partial_{\omega_x}\boldsymbol{\mu}_r\right)^2}{1-\mu^2}. \tag{A5}$$

On the other hand,

$$\partial_{\omega_x}\left|\frac{1+\mu}{2}\right\rangle = \partial_{\omega_x}\theta\,\frac{1}{2}\left(-\sin\left(\frac{\theta}{2}\right)|\uparrow\rangle + \mathrm{e}^{i\varphi}\cos\left(\frac{\theta}{2}\right)|\downarrow\rangle\right) + i\partial_{\omega_x}\varphi\,\mathrm{e}^{i\varphi}\sin\left(\frac{\theta}{2}\right)|\downarrow\rangle \tag{A6}$$

$$= \mathrm{e}^{i\varphi}\left(-\frac{1}{2}\partial_{\omega_x}\theta\left|\frac{1-\mathfrak{p}}{2}\right\rangle + i\partial_{\omega_x}\varphi\,\sin\left(\frac{\theta}{2}\right)|\downarrow\rangle\right), \tag{A7}$$

$$\partial_{\omega_x}\left|\frac{1-\mu}{2}\right\rangle = \partial_x\theta\,\frac{1}{2}\left(\mathrm{e}^{-i\varphi}\cos\left(\frac{\theta}{2}\right)|\uparrow\rangle + \sin\left(\frac{\theta}{2}\right)|\downarrow\rangle\right) - i\partial_{\omega_x}\varphi\,\mathrm{e}^{-i\varphi}\sin\left(\frac{\theta}{2}\right)|\uparrow\rangle \tag{A8}$$

$$= \mathrm{e}^{-i\varphi}\left(\frac{1}{2}\partial_{\omega_x}\theta\left|\frac{1+\mu}{2}\right\rangle - i\partial_{\omega_x}\varphi\,\sin\left(\frac{\theta}{2}\right)|\downarrow\rangle\right), \tag{A9}$$

where [using $2\sin(\theta/2)\cos(\theta/2) = \sin(\theta)$],

$$\left|\left\langle\frac{1\mp\mu}{2}\right|\partial_{\omega_x}\left|\frac{1\pm\mu}{2}\right\rangle\right|^2 = \frac{1}{4}\left[\left(\partial_{\omega_x}\theta\right)^2 + \sin^2\theta\left(\partial_{\omega_x}\varphi\right)^2\right]. \tag{A10}$$

Considering also that

$$\frac{\left(\frac{1\pm\mu}{2}-\frac{1\mp\mu}{2}\right)^2}{\frac{1\pm\mu}{2}+\frac{1\mp\mu}{2}} = \mu^2, \tag{A11}$$

the second term takes from Eq. (4) the form

$$2\sum_{n\neq m}\frac{(\lambda_n-\lambda_m)^2}{\lambda_n+\lambda_m}\left|\langle\lambda_m|\,\partial_{\omega_x}\,|\lambda_n\rangle\right|^2 = \tag{A12}$$

$$\mu^2\left[(\partial_{\omega_x}\theta)^2 + \sin^2\theta(\partial_{\omega_x}\varphi)^2\right] = \left(\partial_{\omega_x}\boldsymbol{\mu}_t\right)^2. \tag{A13}$$

Finally, combining all the expressions, we arrive at Eq. (6)

$$\mathcal{F}_{\mathcal{Q}}(\omega_x) = \frac{1}{1-\mu^2}\left(\partial_{\omega_x}\boldsymbol{\mu}_r\right)^2 + \left(\partial_{\omega_x}\boldsymbol{\mu}_t\right)^2. \tag{A14}$$

APPENDIX B: QUANTUM FISHER INFORMATION FOR PROJECTIVE MEASUREMENTS

Considering Eqs. (7) and (11), we can write the derivative as

$$\partial_{\omega_x}\boldsymbol{\mu}(n\tau+\Delta t) = \tag{B1}$$

$$\mu_0\left[n(\alpha(\tau))^{n-1}\partial_{\omega_x}\alpha(\tau)\boldsymbol{\mu}(\Delta t) + (\alpha(\tau))^n\partial_{\omega_x}\boldsymbol{\mu}(\Delta t)\right]. \tag{B2}$$

Given that $\boldsymbol{\mu}(t)$ is a unit vector for all ω_x, $\boldsymbol{\mu}\cdot\partial_{\omega_x}\boldsymbol{\mu} = 0$. This implies that the squares of the radial and tangential components are

$$\left(\partial_{\omega_x}\boldsymbol{\mu}_r\right)^2 = \mu_0^2 n^2(\alpha(\tau))^{2(n-1)}(\partial_{\omega_x}\alpha(\tau))^2, \tag{B3}$$

$$\left(\partial_{\omega_x}\boldsymbol{\mu}_t\right)^2 = \mu_0^2(\alpha(\tau))^{2n}\left(\partial_{\omega_x}\boldsymbol{\mu}(\Delta t)\right)^2. \tag{B4}$$

The QFI is is then given by

$$\mathcal{F}_{\mathcal{Q}}(\omega_x) = \mu_0^2 n^2 \frac{(\alpha(\tau))^{2(n-1)}}{1-\mu_0^2(\alpha(\tau))^{2n}} \left(\partial_{\omega_x}\alpha(\tau)\right)^2 + \mu_0^2(\alpha(\tau))^{2n}\left(\partial_{\omega_x}\boldsymbol{\mu}(\Delta t)\right)^2, \tag{B5}$$

where

$$(\partial_{\omega_x}\alpha(\tau))^2 = \left(\frac{\omega_x}{\omega}\right)^2\left[2\frac{\omega_z^2}{\omega^3}(1-\cos(\omega\tau)) + \frac{\omega_x^2}{\omega^2}\tau\sin(\omega\tau)\right]^2, \tag{B6}$$

$$\left(\partial_{\omega_x}\boldsymbol{\mu}(\Delta t)\right)^2 = \frac{\omega_x^4}{\omega^4}\Delta t^2 + 2\frac{\omega_x^2\omega_z^2}{\omega^5}\sin(\omega\Delta t)\,\Delta t \tag{B7}$$

$$+ \frac{\omega_z^2}{\omega^4}\left[(1-\cos(\omega\Delta t))^2 + \frac{\omega_z^2}{\omega^2}\sin^2(\omega\Delta t)\right]. \tag{B8}$$

The first term is constant as a function of the time between measurements Δt, and the second term is bounded by $\mu_0^2(\alpha(\tau))^{2n}\max_{\Delta t\in[0,\tau)}\left(\partial_{\omega_x}\boldsymbol{\mu}(\Delta t)\right)^2$. At the projected measurement times $t = n\tau$, the first term of Eq. (B5) becomes Eq. (13).

[1] C. A. Meriles, L. Jiang, G. Goldstein, J. S. Hodges, J. Maze, M. D. Lukin, and P. Cappellaro, Imaging mesoscopic nuclear spin noise with a diamond magnetometer, J. Chem. Phys. **133**, 124105 (2010).

[2] I. Almog, Y. Sagi, G. Gordon, G. Bensky, G. Kurizki, and N. Davidson, Direct measurement of the system–environment coupling as a tool for understanding decoherence and dynamical decoupling, J. Phys. B: At., Mol. Opt. Phys. **44**, 154006 (2011).

[3] J. Bylander, S. Gustavsson, F. Yan, F. Yoshihara, K. Harrabi, G. Fitch, D. G. Cory, Y. Nakamura, J. Tsai, and W. D. Oliver, Noise spectroscopy through dynamical decoupling with a superconducting flux qubit, Nat. Phys. **7**, 565 (2011).

[4] G. A. Álvarez and D. Suter, Measuring the spectrum of colored noise by dynamical decoupling, Phys. Rev. Lett. **107**, 230501 (2011).

[5] P. E. S. Smith, G. Bensky, G. A. Álvarez, G. Kurizki, and L. Frydman, Shift-driven modulations of spin-echo signals, Proc. Natl. Acad. Sci. USA **109**, 5958 (2012).

[6] C. O. Bretschneider, G. A. Álvarez, G. Kurizki, and L. Frydman, Controlling spin-spin network dynamics by repeated projective measurements, Phys. Rev. Lett. **108**, 140403 (2012).

[7] L. Cywinski, Dynamical-decoupling noise spectroscopy at an optimal working point of a qubit, Phys. Rev. A **90**, 042307 (2014).

[8] D. Suter and G. A. Álvarez, Colloquium: Protecting quantum information against environmental noise, Rev. Mod. Phys. **88**, 041001 (2016).

[9] A. Zwick, G. A. Álvarez, and G. Kurizki, Maximizing information on the environment by dynamically controlled qubit probes, Phys. Rev. Appl. **5**, 014007 (2016).

[10] A. Zwick, G. A. Álvarez, and G. Kurizki, Criticality of environmental information obtainable by dynamically controlled quantum probes, Phys. Rev. A **94**, 042122 (2016).

[11] C. L. Degen, F. Reinhard, and P. Cappellaro, Quantum sensing, Rev. Mod. Phys. **89**, 035002 (2017).

[12] F. Poggiali, P. Cappellaro, and N. Fabbri, Optimal control for one-qubit quantum sensing, Phys. Rev. X **8**, 021059 (2018).

[13] A. Zwick, D. Suter, G. Kurizki, and G. A. Álvarez, Precision limits of tissue microstructure characterization by magnetic resonance imaging, Phys. Rev. Appl. **14**, 024088 (2020).

[14] A. Zwick and G. A. Álvarez, Quantum sensing tools to characterize physical, chemical and biological processes with magnetic resonance, J. Magn. Reson. Open **16–17**, 100113 (2023).

[15] L.-M. Duan, E. Demler, and M. D. Lukin, Controlling spin exchange interactions of ultracold atoms in optical lattices, Phys. Rev. Lett. **91**, 090402 (2003).

[16] W. S. Bakr, J. I. Gillen, A. Peng, S. Fölling, and M. Greiner, A quantum gas microscope for detecting single atoms in a Hubbard-regime optical lattice, Nature **462**, 74 (2009).

[17] S. Diehl, A. Micheli, A. Kantian, B. Kraus, H. P. Büchler, and P. Zoller, Quantum states and phases in driven open quantum systems with cold atoms, Nat. Phys. **4**, 878 (2008).

[18] P. Jurcevic, B. P. Lanyon, P. Hauke, C. Hempel, P. Zoller, R. Blatt, and C. F. Roos, Quasiparticle engineering and entanglement propagation in a quantum many-body system, Nature **511**, 202 (2014).

[19] E. A. Martinez, C. A. Muschik, P. Schindler, D. Nigg, A. Erhard, M. Heyl, P. Hauke, M. Dalmonte, T. Monz, P. Zoller, and R. Blatt, Real-time dynamics of lattice gauge theories with a few-qubit quantum computer, Nature **534**, 516 (2016).

[20] K. A. Landsman, C. Figgatt, T. Schuster, N. M. Linke, B. Yoshida, N. Y. Yao, and C. Monroe, Verified quantum information scrambling, Nature **567**, 61 (2019).

[21] M. Saffman, T. G. Walker, and K. Molmer, Quantum information with Rydberg atoms, Rev. Mod. Phys. **82**, 2313 (2010).

[22] J. Schachenmayer, B. P. Lanyon, C. F. Roos, and A. J. Daley, Entanglement growth in quench dynamics with variable range interactions, Phys. Rev. X **3**, 031015 (2013).

[23] B. Yan, S. A. Moses, B. Gadway, J. P. Covey, K. R. A. Hazzard, A. M. Rey, D. S. Jin, and J. Ye, Observation of dipolar spin-exchange interactions with lattice-confined polar molecules, Nature **501**, 521 (2013).

[24] J. Zhang, X. Peng, N. Rajendran, and D. Suter, Detection of quantum critical points by a probe qubit, Phys. Rev. Lett. **100**, 100501 (2008).

[25] G. A. Álvarez and D. Suter, NMR quantum simulation of localization effects induced by decoherence, Phys. Rev. Lett. **104**, 230403 (2010).

[26] A. M. Souza, G. A. Álvarez, and D. Suter, Robust dynamical decoupling for quantum computing and quantum memory, Phys. Rev. Lett. **106**, 240501 (2011).
[27] G. A. Álvarez, N. Shemesh, and L. Frydman, Coherent dynamical recoupling of diffusion-driven decoherence in magnetic resonance, Phys. Rev. Lett. **111**, 080404 (2013).
[28] G. A. Álvarez, D. Suter, and R. Kaiser, Localization-delocalization transition in the dynamics of dipolar-coupled nuclear spins, Science **349**, 846 (2015).
[29] X. Yang, J. Thompson, Z. Wu, M. Gu, X. Peng, and J. Du, Probe optimization for quantum metrology via closed-loop learning control, npj Quantum Inf. **6**, 62 (2020).
[30] M. Jiang, Y. Ji, Q. Li, R. Liu, D. Suter, and X. Peng, Multiparameter quantum metrology using strongly interacting spin systems, ArXiv:2104.00211.
[31] R. Fischer, C. O. Bretschneider, P. London, D. Budker, D. Gershoni, and L. Frydman, Bulk nuclear polarization enhanced at room temperature by optical pumping, Phys. Rev. Lett. **111**, 057601 (2013).
[32] T. Staudacher, F. Shi, S. Pezzagna, J. Meijer, J. Du, C. A. Meriles, F. Reinhard, and J. Wrachtrup, Nuclear magnetic resonance spectroscopy on a (5-nanometer)3 sample volume, Science **339**, 561 (2013).
[33] F. Shi, X. Kong, P. Wang, F. Kong, N. Zhao, R.-B. Liu, and J. Du, Sensing and atomic-scale structure analysis of single nuclear-spin clusters in diamond, Nat. Phys. **10**, 21 (2013).
[34] G. Waldherr, Y. Wang, S. Zaiser, M. Jamali, T. Schulte-Herbrüggen, H. Abe, T. Ohshima, J. Isoya, J. F. Du, P. Neumann, and J. Wrachtrup, Quantum error correction in a solid-state hybrid spin register, Nature **506**, 204 (2014).
[35] A. Z. Chaudhry, Utilizing nitrogen-vacancy centers to measure oscillating magnetic fields, Phys. Rev. A **90**, 042104 (2014).
[36] G. A. Álvarez, C. O. Bretschneider, R. Fischer, P. London, H. Kanda, S. Onoda, J. Isoya, D. Gershoni, and L. Frydman, Local and bulk ^{13}C hyperpolarization in nitrogen-vacancy-centred diamonds at variable fields and orientations, Nat. Commun. **6**, 8456 (2015).
[37] T. Staudacher, N. Raatz, S. Pezzagna, J. Meijer, F. Reinhard, C. A. Meriles, and J. Wrachtrup, Probing molecular dynamics at the nanoscale via an individual paramagnetic centre, Nat. Commun. **6**, 8527 (2015).
[38] S. Schmitt, T. Gefen, F. M. Stürner, T. Unden, G. Wolff, C. Müller, J. Scheuer, B. Naydenov, M. Markham, S. Pezzagna, *et al.*, Submillihertz magnetic spectroscopy performed with a nanoscale quantum sensor, Science **356**, 832 (2017).
[39] J. M. Boss, K. Cujia, J. Zopes, and C. L. Degen, Quantum sensing with arbitrary frequency resolution, Science **356**, 837 (2017).
[40] D. R. Glenn, D. B. Bucher, J. Lee, M. D. Lukin, H. Park, and R. L. Walsworth, High-resolution magnetic resonance spectroscopy using a solid-state spin sensor, Nature **555**, 351 (2018).
[41] P. R. Zangara, S. Dhomkar, A. Ajoy, K. Liu, R. Nazaryan, D. Pagliero, D. Suter, J. A. Reimer, A. Pines, and C. A. Meriles, Dynamics of frequency-swept nuclear spin optical pumping in powdered diamond at low magnetic fields, Proc. Natl. Acad. Sci. **116**, 2512 (2019).
[42] M. Yu, D. Li, J. Wang, Y. Chu, P. Yang, M. Gong, N. Goldman, and J. Cai, Experimental estimation of the quantum Fisher information from randomized measurements, Phys. Rev. Res. **3**, 043122 (2021).
[43] Z. Jiang, H. Cai, R. Cernansky, X. Liu, and W. Gao, Quantum sensing of radio-frequency signal with NV centers in SiC, Sci. Adv. **9**, eadg2080 (2023).
[44] T. F. Segawa and R. Igarashi, Nanoscale quantum sensing with nitrogen-vacancy centers in nanodiamonds—A magnetic resonance perspective, Prog. Nucl. Magn. Reson. Spectrosc. **134**, 20 (2023).
[45] L. D. Landau and E. M. Lifshitz, *Quantum Mechanics: Non-Relativistic Theory* (Pergamon Press, Oxford, 1977), Vol. 3.
[46] J. E. Lang, R. B. Liu, and T. S. Monteiro, Dynamical-decoupling-based quantum sensing: Floquet spectroscopy, Phys. Rev. X **5**, 041016 (2015).
[47] A. N. Pravdivtsev, A. V. Yurkovskaya, R. Kaptein, K. Miesel, H.-M. Vieth, and K. L. Ivanov, Exploiting level anti-crossings for efficient and selective transfer of hyperpolarization in coupled nuclear spin systems, Phys. Chem. Chem. Phys. **15**, 14660 (2013).
[48] A. N. Pravdivtsev, A. V. Yurkovskaya, N. N. Lukzen, H.-M. Vieth, and K. L. Ivanov, Exploiting level anti-crossings (LACs) in the rotating frame for transferring spin hyperpolarization, Phys. Chem. Chem. Phys. **16**, 18707 (2014).
[49] K. L. Ivanov, A. N. Pravdivtsev, A. V. Yurkovskaya, H.-M. Vieth, and R. Kaptein, The role of level anti-crossings in nuclear spin hyperpolarization, Prog. Nucl. Magn. Reson. Spectrosc. **81**, 1 (2014).
[50] A. N. Pravdivtsev, A. V. Yurkovskaya, N. N. Lukzen, K. L. Ivanov, and H.-M. Vieth, Highly efficient polarization of spin-1/2 insensitive NMR nuclei by adiabatic passage through level anticrossings, J. Phys. Chem. Lett. **5**, 3421 (2014).
[51] J. P. King, K. Jeong, C. C. Vassiliou, C. S. Shin, R. H. Page, C. E. Avalos, H.-J. Wang, and A. Pines, Room-temperature in situ nuclear spin hyperpolarization from optically pumped nitrogen vacancy centres in diamond, Nat. Commun. **6**, 1 (2015).
[52] K. R. K. Rao and D. Suter, Level anti-crossings of a nitrogen-vacancy center in diamond: Decoherence-free subspaces and 3D sensors of microwave magnetic fields, New J. Phys. **22**, 103065 (2020).
[53] H.-J. Wang, C. S. Shin, C. E. Avalos, S. J. Seltzer, D. Budker, A. Pines, and V. S. Bajaj, Sensitive magnetic control of ensemble nuclear spin hyperpolarization in diamond, Nat. Commun. **4**, 1 (2013).
[54] D. A. Broadway, J. D. Wood, L. T. Hall, A. Stacey, M. Markham, D. A. Simpson, J.-P. Tetienne, and L. C. Hollenberg, Anticrossing spin dynamics of diamond nitrogen-vacancy centers and all-optical low-frequency magnetometry, Phys. Rev. Appl. **6**, 064001 (2016).
[55] A. Ajoy, K. Liu, R. Nazaryan, X. Lv, P. R. Zangara, B. Safvati, G. Wang, D. Arnold, G. Li, A. Lin, *et al.*, Orientation-independent room temperature optical ^{13}C hyperpolarization in powdered diamond, Sci. Adv. **4**, eaar5492 (2018).
[56] M. Onizhuk, K. C. Miao, J. P. Blanton, H. Ma, C. P. Anderson, A. Bourassa, D. D. Awschalom, and G. Galli,

Probing the coherence of solid-state qubits at avoided crossings, PRX Quantum **2**, 010311 (2021).
[57] S. Pang and A. N. Jordan, Optimal adaptive control for quantum metrology with time-dependent hamiltonians, Nat. Commun. **8**, 14695 (2017).
[58] M. P. V. Stenberg, Y. R. Sanders, and F. K. Wilhelm, Efficient estimation of resonant coupling between quantum systems, Phys. Rev. Lett. **113**, 210404 (2014).
[59] A. H. Kiilerich and K. Mølmer, Quantum Zeno effect in parameter estimation, Phys. Rev. A **92**, 032124 (2015).
[60] T. Joas, S. Schmitt, R. Santagati, A. A. Gentile, C. Bonato, A. Laing, L. P. McGuinness, and F. Jelezko, Online adaptive quantum characterization of a nuclear spin, npj Quantum Inf. **7**, 1 (2021).
[61] F. M. Ciurana, G. Colangelo, L. Slodička, R. Sewell, and M. Mitchell, Entanglement-enhanced radio-frequency field detection and waveform sensing, Phys. Rev. Lett. **119**, 043603 (2017).
[62] U. Mishra and A. Bayat, Integrable quantum many-body sensors for ac field sensing, Sci. Rep. **12**, 14760 (2022).
[63] M. Kuffer, A. Zwick, and G. A. Álvarez, Path integral framework for characterizing and controlling decoherence induced by nonstationary environments on a quantum probe, PRX Quantum **3**, 020321 (2022).
[64] C.-W. Kiang, J.-J. Ding, and J.-F. Kiang, Quantum sensing of fast time-varying magnetic field with daubechies wavelets, IEEE Access **12**, 23181 (2024).
[65] M. Kuffer, A. Zwick, and G. A. Álvarez, Sensing out-of-equilibrium and quantum non-Gaussian environments via induced time-reversal symmetry breaking on the quantum-probe dynamics, ArXiv:2405.04742.
[66] S. L. Braunstein and C. M. Caves, Statistical distance and the geometry of quantum states, Phys. Rev. Lett. **72**, 3439 (1994).
[67] M. G. A. Paris, Quantum estimation for quantum technology, Int. J. Quantum Inf. **07**, 125 (2009).
[68] B. M. Escher, R. L. de Matos Filho, and L. Davidovich, General framework for estimating the ultimate precision limit in noisy quantum-enhanced metrology, Nat. Phys. **7**, 406 (2011).
[69] C. Benedetti and M. G. A. Paris, Characterization of classical Gaussian processes using quantum probes, Phys. Lett. A **378**, 2495 (2014).
[70] C. Benedetti, F. Salari Sehdaran, M. H. Zandi, and M. G. A. Paris, Quantum probes for the cutoff frequency of Ohmic environments, Phys. Rev. A **97**, 012126 (2018).
[71] V. Mukherjee, A. Zwick, A. Ghosh, X. Chen, and G. Kurizki, Enhanced precision bound of low-temperature quantum thermometry via dynamical control, Commun. Phys. **2**, 162 (2019).
[72] H. Ather and A. Z. Chaudhry, Improving the estimation of environment parameters via initial probe-environment correlations, Phys. Rev. A **104**, 012211 (2021).
[73] P. G. Kwiat, A. White, J. Mitchell, O. Nairz, G. Weihs, H. Weinfurter, and A. Zeilinger, High-efficiency quantum interrogation measurements via the quantum Zeno effect, Phys. Rev. Lett. **83**, 4725 (1999).
[74] A. G. Kofman and G. Kurizki, Acceleration of quantum decay processes by frequent observations, Nature **405**, 546 (2000).
[75] M. M. Müller, S. Gherardini, and F. Caruso, Stochastic quantum Zeno-based detection of noise correlations, Sci. Rep. **6**, 1 (2016).
[76] M. M. Müller, S. Gherardini, N. Dalla Pozza, and F. Caruso, Noise sensing via stochastic quantum Zeno, Phys. Lett. A **384**, 126244 (2020).
[77] B. Misra and E. C. G. Sudarshan, The Zeno's paradox in quantum theory, J. Math. Phys. **18**, 756 (1977).
[78] H.-V. Do, C. Lovecchio, I. Mastroserio, N. Fabbri, F. S. Cataliotti, S. Gherardini, M. M. Müller, N. Dalla Pozza, and F. Caruso, Experimental proof of quantum Zeno-assisted noise sensing, New J. Phys. **21**, 113056 (2019).
[79] S. Virzi, A. Avella, F. Piacentini, M. Gramegna, T. Opatrný, A. G. Kofman, G. Kurizki, S. Gherardini, F. Caruso, I. P. Degiovanni, and M. Genovese, Quantum zeno and anti-Zeno probes of noise correlations in photon polarization, Phys. Rev. Lett. **129**, 030401 (2022).
[80] G. Kurizki, A. G. Kofman, and V. Yudson, Resonant photon exchange by atom pairs in high-Q cavities, Phys. Rev. A **53**, R35 (1996).
[81] N. Erez, G. Gordon, M. Nest, and G. Kurizki, Thermodynamic control by frequent quantum measurements, Nature **452**, 724 (2008).
[82] G. A. Álvarez, D. D. B. Rao, L. Frydman, and G. Kurizki, Zeno and anti-Zeno polarization control of spin ensembles by induced dephasing, Phys. Rev. Lett. **105**, 160401 (2010).
[83] D. B. R. Dasari, S. Yang, A. Chakrabarti, A. Finkler, G. Kurizki, and J. Wrachtrup, Anti-Zeno purification of spin baths by quantum probe measurements, Nat. Commun. **13**, 7527 (2022).
[84] S.-I. Amari, *Information Geometry and Its Applications* (Springer, Tokio Japan, 2016), Vol. 194.
[85] J.-F. Wang, F.-F. Yan, Q. Li, Z.-H. Liu, H. Liu, G.-P. Guo, L.-P. Guo, X. Zhou, J.-M. Cui, J. Wang, *et al.*, Coherent control of nitrogen-vacancy center spins in silicon carbide at room temperature, Phys. Rev. Lett. **124**, 223601 (2020).
[86] Z. Mu, S. A. Zargaleh, H. J. von Bardeleben, J. E. Fröch, M. Nonahal, H. Cai, X. Yang, J. Yang, X. Li, I. Aharonovich, *et al.*, Coherent manipulation with resonant excitation and single emitter creation of nitrogen vacancy centers in 4H silicon carbide, Nano Lett. **20**, 6142 (2020).
[87] J. Dalibard, Y. Castin, and K. Mölmer, Wave-function approach to dissipative processes in quantum optics, Phys. Rev. Lett. **68**, 580 (1992).
[88] M. A. Nielsen, E. Knill, and R. Laflamme, Complete quantum teleportation using nuclear magnetic resonance, Nature **396**, 52 (1998).
[89] G. Teklemariam, E. M. Fortunato, C. C. López, J. Emerson, J. P. Paz, T. F. Havel, and D. G. Cory, Method for modeling decoherence on a quantum-information processor, Phys. Rev. A **67**, 062316 (2003).
[90] R. Tycko, Stochastic dipolar recoupling in nuclear magnetic resonance of solids, Phys. Rev. Lett. **99**, 187601 (2007).
[91] W. Zheng, D. Z. Xu, X. Peng, X. Zhou, J. Du, and C. P. Sun, Experimental demonstration of the quantum Zeno effect in NMR with entanglement-based measurements, Phys. Rev. A **87**, 032112 (2013).

[92] L. Xiao and J. A. Jones, NMR analogues of the quantum Zeno effect, Phys. Lett. A **359**, 424 (2006).

[93] G. Kurizki and A. Zwick, in *Adv. Chem. Phys. 159*, edited by P. Brumer, S. A. Rice, and A. R. Dinner (Wiley, Hoboken, New Jersey, U.S., 2016), http://eu.wiley.com/WileyCDA/WileyTitle/productCd-9781119096269.html.

[94] D. Cory, R. Laflamme, E. Knill, L. Viola, T. Havel, N. Boulant, G. Boutis, E. Fortunato, S. Lloyd, R. Martinez, C. Negrevergne, M. Pravia, Y. Sharf, G. Teklemariam, Y. Weinstein, and W. Zurek, NMR based quantum information processing: Achievements and prospects, Fortschr. Phys. **48**, 875 (2000).

[95] A. M. Souza, G. A. Álvarez, and D. Suter, Robust dynamical decoupling, Phil. Trans. R. Soc. A **370**, 4748 (2012).

[96] C. P. Slichter, *Principles of Magnetic Resonance* (Springer-Verlag Berlin Heidelberg, Berlin, Heidelberg, 1990).

[97] J. Perlo, V. Demas, F. Casanova, C. A. Meriles, J. Reimer, A. Pines, and B. Blümich, High-resolution NMR spectroscopy with a portable single-sided sensor, Science **308**, 1279 (2005).

[98] L. Braunschweiler and R. Ernst, Coherence transfer by isotropic mixing: application to proton correlation spectroscopy, J. Magn. Reson. (1969) **53**, 521 (1983).

[99] P. Caravatti, L. Braunschweiler, and R. Ernst, Heteronuclear correlation spectroscopy in rotating solids, Chem. Phys. Lett. **100**, 305 (1983).

[100] R. R. Ernst, G. Bodenhausen, and A. Wokaun, *Principles of Nuclear Magnetic Resonance in One and Two Dimensions* (Oxford University Press, USA, 1990).

[101] B. Luy, O. Schedletzky, and S. J. Glaser, Analytical polarization transfer functions for four coupled spins12under isotropic mixing conditions, J. Magn. Reson. **138**, 19 (1999).

[102] A. K. Chattah, G. A. Álvarez, P. R. Levstein, F. M. Cucchietti, H. M. Pastawski, J. Raya, and J. Hirschinger, Many-spin quantum dynamics during cross polarization in 8CB, J. Chem. Phys. **119**, 7943 (2003).

[103] G. A. Álvarez, E. P. Danieli, P. R. Levstein, and H. M. Pastawski, Environmentally induced quantum dynamical phase transition in the spin swapping operation, J. Chem. Phys. **124**, 194507 (2006).

[104] J. Raya, B. Perrone, B. Bechinger, and J. Hirschinger, Chemical shift powder spectra obtained by using rotor-directed exchange of orientations cross-polarization (rodeo-cp), Chem. Phys. Lett. **508**, 155 (2011).

[105] K. J. Harris, A. Lupulescu, B. E. Lucier, L. Frydman, and R. W. Schurko, Broadband adiabatic inversion pulses for cross polarization in wideline solid-state NMR spectroscopy, J. Magn. Reson. **224**, 38 (2012).

[106] J. Raya, B. Perrone, and J. Hirschinger, Chemical shift powder spectra enhanced by multiple-contact cross-polarization under slow magic-angle spinning, J. Magn. Reson. **227**, 93 (2013).

[107] J. Raya and J. Hirschinger, Sensitivity enhancement by multiple-contact cross-polarization under magic-angle spinning, J. Magn. Reson. **281**, 253 (2017).

[108] J. Hirschinger and J. Raya, Analytical descriptions of (multiple-contact) cross-polarization dynamics and spin-lattice relaxation in solid alanine, J. Magn. Reson. Open **16**, 100128 (2023).

[109] L. Müller, A. Kumar, T. Baumann, and R. R. Ernst, Transient oscillations in NMR cross-polarization experiments in solids, Phys. Rev. Lett. **32**, 1402 (1974).

[110] S. R. Hartmann and E. L. Hahn, Nuclear double resonance in the rotating frame, Phys. Rev. **128**, 2042 (1962).

[111] G. A. Álvarez, E. P. Danieli, P. R. Levstein, and H. M. Pastawski, Decoherence under many-body system-environment interactions: A stroboscopic representation based on a fictitiously homogenized interaction rate, Phys. Rev. A **75**, 062116 (2007).

[112] E. Ferraro, M. Scala, R. Migliore, and A. Napoli, On the validity of non-Markovian master equation approaches for the entanglement dynamics of two-qubit systems, Phys. Scr. **T140**, 014042 (2010).

[113] H. M. Pastawski and E. Medina, "Tight binding" methods in quantum transport through molecules and small devices: From the coherent to the decoherent description, Rev. Mex. Fisica **47s1**, 1 (2001).